SCIENCE OF **TSUNAMI HAZARDS**

Journal of Tsunami Society International

Volume 37 **Number 4** **2018**

SOURCE PARAMETER ESTIMATES OF THE 4 NOVEMBER 2016 m_b= 4.7 EARTHQUAKE NEAR LAWU MOUNTAIN IN EAST JAVA, INDONESIA 222

Madlazim[1,2] and T. Prastowo[1,2]

1 Physics Department, Faculty of Mathematics and Natural Sciences, Universitas Negeri Surabaya, Kampus Unesa Ketintang, Surabaya 60231, **INDONESIA**

2 Center for Earth Science Studies, Faculty of Mathematics and Natural Sciences, Universitas Negeri Surabaya, Kampus Unesa Ketintang, Surabaya 60231, **INDONESIA**

TSUNAMI SOCIETY INTERNATIONAL, 1741 Ala Moana Blvd. #70, Honolulu, HI 96815, USA.

SCIENCE OF TSUNAMI HAZARDS is a CERTIFIED OPEN ACCESS Journal included in the prestigious international academic journal database DOAJ, maintained by the University of Lund in Sweden with the support of the European Union. SCIENCE OF TSUNAMI HAZARDS is also preserved, archived and disseminated by the National Library, The Hague, NETHERLANDS, the Library of Congress, Washington D.C., USA, the Electronic Library of Los Alamos, National Laboratory, New Mexico, USA, the EBSCO Publishing databases and ELSEVIER Publishing in Amsterdam. The vast dissemination gives the journal additional global exposure and readership in 90% of the academic institutions worldwide, including nation-wide access to databases in more than 70 countries.

OBJECTIVE: Tsunami Society International publishes this interdisciplinary journal to increase and disseminate knowledge about tsunamis and their hazards.

DISCLAIMER: Although the articles in SCIENCE OF TSUNAMI HAZARDS have been technically reviewed by peers, Tsunami Society International is not responsible for the veracity of any statement, opinion or consequences.

Submit manuscripts of research papers, notes or letters to the Editor. If a research paper is accepted for publication the author(s) must submit a scan-ready manuscript, a Doc, TeX or a PDF file in the journal format. Issues of the journal are published electronically in PDF format. There is a minimal publication fee for authors who are members of Tsunami Society International for three years and slightly higher for non-members. Tsunami Society International members are notified by e-mail when a new issue is available. Permission to use figures, tables and brief excerpts from this journal in scientific and educational works is granted provided that the source is acknowledged.

Recent and all past journal issues are available at: http://www.TsunamiSociety.org CD-ROMs of past volumes may be purchased by contacting Tsunami Society International at postmaster@tsunamisociety.org Issues of the journal from 1982 thru 2005 are also available in PDF format at the U.S. Los Alamos National Laboratory Library http://epubs.lanl.gov/tsunami/

ISSN 8755-6839

SCIENCE OF **TSUNAMI HAZARDS**

Journal of Tsunami Society International

Volume 37 **Number 4** **2018**

TSUNAMI EVACUATION PLAN FOR THE CITY OF TANGIER-MOROCCO BASED ON GIS TOOLS

Sabah Benchekroun [1] and Azelarab El Mouraouah [2]

[1] Centre National pour la Recherche Scientifique et Technique (CNRST), Angle avenue Allal El Fassi et avenue des FAR, Hay Ryad. BP. 8027, 10102 - Rabat, Morocco,

[2] Université Mohammed V, Institut Scientifique, Laboratoire de Physique du Globe. B.P. 703 Agdal, Rabat, Morocco .

ABSTRACT

Morocco is located in convergence zone between two major plates, the Eurasian and the African plates. Moroccan coastal regions are prone to tsunami hazard caused by major earthquakes located along this boundary. The rapid growth of population and expansion in infrastructures and economic settlements in Moroccan coastal areas make them more vulnerable to tsunami threat. Tsunami evacuation plan is an important tool to mitigate the tsunami impact, it's the most efficient way to save human lives before the waves reach the hazard zone areas. In this study, we propose a tsunami evacuation plan for the city of Tangier-Morocco for horizontal evacuation. This plan is designed considering the tsunami threat from tsunamigenic source located in the SW Iberian margin and using the inundation maps of the worst case scenario to define the flooding area. The evacuation plan is elaborated through modeling evacuation routes using Closet Facility tool implemented in ESRIS's ArcMap 10.2 geographic information system (GIS) software. The proposed evacuation plan give valuable information to local government authorities and emergency managers in order to implement an official evacuation plan for Tangier city. It also provides practical support to increase community resilience.

Keywords: *tsunami, worst case scenario, geographic information system (GIS), inundation map, evacuation plan.*

Vol 37. No. 4, page 157 (2018)

1. INTRODUCTION

Morocco is located near the Azores-Gilbraltar Fracture Zone (AGFZ), which marks the boundary of active tectonic interaction between the African and the Eurasian plates where major earthquakes can occur. The most destructive historical tsunamigenic earthquake near AGFZ occurred at 9:40 in the morning of 1 November 1775 (Fig.1). There were three distinct shocks over a ten minute period. The first shock was followed by an even more powerful second shock which destroyed many buildings in Lisbon and other cities in Portugal. According to reports, the tremors and ground motions lasted for three-and-one-half minutes. The first of the tsunami waves reached Lisbon about 40 minutes afterwards and in less than an hour reached Morocco. In Gibraltar, the sea rose suddenly by about two meters. The greater damage and casualties occurred on the western coast from Tangier, where the waves reached the walled fortifications of the town, to Agadir where the waters passed over the walls, killing many. The earthquake and the tsunami were particularly destructive in Morocco, where approximately 10,000 people lost their lives. Archival records document that the coastal towns of Rabat, Larache, Asilah, and Agadir (named Santa Cruz at that time) suffered much damage (Pararas-Carayannis, 2001). Another potential tsunamigenic area is south of the Gorringe bank near the Azores-Gibraltar fracture zone where an event occurred in 1969. It is expected that tsunamis will strike again Morocco, so a program of preparedness is an absolute necessity.

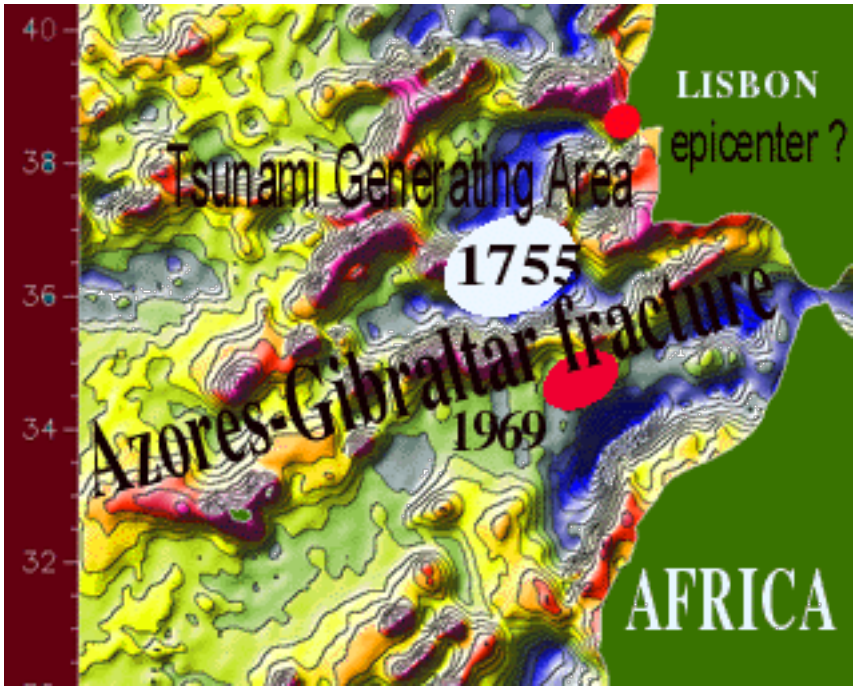

Fig.1 Generating Areas of the 1755 and 1969 tsunamis along the Azores-Gibraltar Fracture Zone (AGFZ) superimposed on bathymetry and gravity anomaly map (Source: Pararas-Carayannis, 2001)

A Tsunami Evacuation Plan is considered as a fundamental tool to mitigate the risk and save lives. Indeed, evacuation of vulnerable areas remains the most efficient action to save lives before the tsunami waves arrive. The Plan requires rapid evacuation of people from danger zones of coastal communities. The disastrous tsunami that struck the eastern coast of Japan on 11 March 2011, generated by the great Tohoku-Oki earthquake, (Mw 9.0), indicated that even the most protective tsunami structures (protective walls, fences, etc) were overtopped by waves (Pararas-Carayannis, 2011 a, b, 2014; Mas et al., 2012,). "Evacuation procedures" to a safer place provide the only effective way of moving people away from a potential danger area.

The present study proposes a simple methodology to evacuate effectively Tangier residents from tsunami prone areas to buildings, shelters and assembly areas in safe zones. Routes are modeled using Closet Facility tool implemented in ESRIS's ArcMap 10.2 geographic information system (GIS) software. This tool is used in network analysis in order to measure the cost of traveling between input sites (incidents) and locations (facilities). It's used for finding the locations based on the impedance chosen (time, distance etc...). In this study, we try to obtain the shortest path taking account the walking speed of evacuees and the capacity (width) of the road network. The Closet Facility tool, considered as macro-simulator approach, has the advantage to not require a lot of calculation and the results are easily exploitable in any Geographic Information System (GIS). The proposed map could be used by the local authorities in the process of evacuation in case of tsunami warning, it also helps to prepare and raise awareness among the populations living in tsunami hazard area.

2. BRIEF OVERVIEW OF TSUNAMI EVACUATION MODELING

In order to quantify the evacuation time, several studies have focused on developing different evacuation models. Pidd et al. (1996) distinguished two models to simulate tsunami evacuations: macro-simulators and micro-simulators. These models differ on spatial scale and variables taken into account. The macro-simulators have the interest of assessing "absolute" accessibility to refuge sites regardless of individual behavior, while the micro-simulators are considered as a dynamic approach, they try to assess "relative" accessibility taking into account human behavior with several individual characteristics and their interactions. However, we note the complementary of these two approaches.

The micro-simulator models require efficient capacity and very long calculation times, they are mainly applied in evacuations within buildings (malls, big hotels, stadiums ...) or in ships like the study conducted by Klüpfel et al. (2000). There are several types of micro-simulators models to simulate pedestrian evacuation in case of tsunami, the most known are: i) the "Multi-Agent System (MAS)" model; during the modeling, each agent maximizes his personal evacuation route to find the way of the faster evacuation. This method has been successfully applied to the town of Aonae (Okushiri Island, Hokkaido Japan) by Saito and Kagami (2004) using the software MAS (Multi Agent Simulator), to Padang city in Indonesia by Lammel et al. (2008) using MATsim (Multi-Agent Traffic

simulation) software and recently to Arahama town located near the Sendai city, Japan by Mas et al. (2012). ii) the "Automate Cellular (AC)" model which was used for the first time in road traffic simulation by Nagel and Schreckenberg (1992). It is generally applied to model complex dynamic systems and iii) the "Social Force" model developed by Helbing and Molnar (1995). This model considers the behavior of each pedestrian which is affected by internal forces (the willpower to reach the destination) and by external ones due to others pedestrians (socio-psychological and physical influences) or to the obstacles present in his environment. The "SimWalk" is one of the software's based on "Social Force" model, it was applied by Steiner et al.(2007).

The macro-simulators models are used at more large scale. This approach has a static setting, it calculates the travel time in wide and open areas and describes each part of the space by attributes that take into account the speed of pedestrians. The approach, based on the shortest path theory associated with a GIS, was developed by Hamacher and Tjandra (2001), it has the advantage of not dealing with phenomena that are often random and complex.

This type of simulations are used to select large-scale evacuation routes. Several programs have been developed like : i) ETR (Evacuation Route Tools) that was developed as a part of the CRATER program (Coastal Risk Analysis and Environmental Remediation of Tsunamis, 2005) and which was applied in Thailand (Phuket Province and Phang Nga Province) ii) "Route Finder" was developed in MapInfo GIS platform. It has been widely applied in various places such as Indonesia in Mayotte (Leone et al. 2013), in the French Riviera (Sahal et al., 2013) and Martinique (Péroche et al., 2014). This application has the advantage of being easily transferable to different sites iii) "CASPER" (Capacity Aware Routing Evacuation Shortest Path) a tool developed for ArcGIS Network Analyst by (Shahabi and Wilson, 2014) and iv) least-cost-distance (LCD) model implemented in ArcMap, this model takes into account the slope and land cover of an area, it was applied in Aberdeen, Hoquiam, and Cosmopolis cities in the U.S. Pacific Northwest by Wood et al (2016) .

3. METHODOLOGY

Before launching the modeling of the shortest roads by "Closet Facility" tool, many GIS datasets should be configurated and created. These dataset are used as input, it includes many steps (Fig. 2);

Determination of danger areas and safe areas : danger areas correspond to the flooded areas estimated by tsunami hazard study. The inundated zone is the result of the determination of the potential of tsunamigenic sources and the use of numerical modeling. The obtained tsunami hazard map gives an idea of the limit of the inundated area which should be evacuated in case of tsunami warning. All areas located outside the inundation zone (generally located above than 20m) are considered as safe areas.

- Estimation of exposed population: to simulate the evacuation routes, it is essential to know the number of population (residents or not) present in the potential tsunami flooded zone and their distribution. The number of people to evacuate affects road capacity, also, locations of evacuees are taken as starting points for modeling.

Construction of road network dataset: the object of this step is to built a road network taking into account surface condition, slope, length and capacity of the paths (width). Road network is very essential for evacuation purposes since it will determine the movement of evacuees along the evacuation routes and also serves as connections to the evacuation building shelters.

Identification of assembly areas or evacuation building shelters: these buildings are selected according to the best practice guidelines set out in FEMA (2009). Building shelters or Assembly areas are chosen related to their locations, capacity, accessibility using the road network and the safety after a preceding local or regional earthquake.

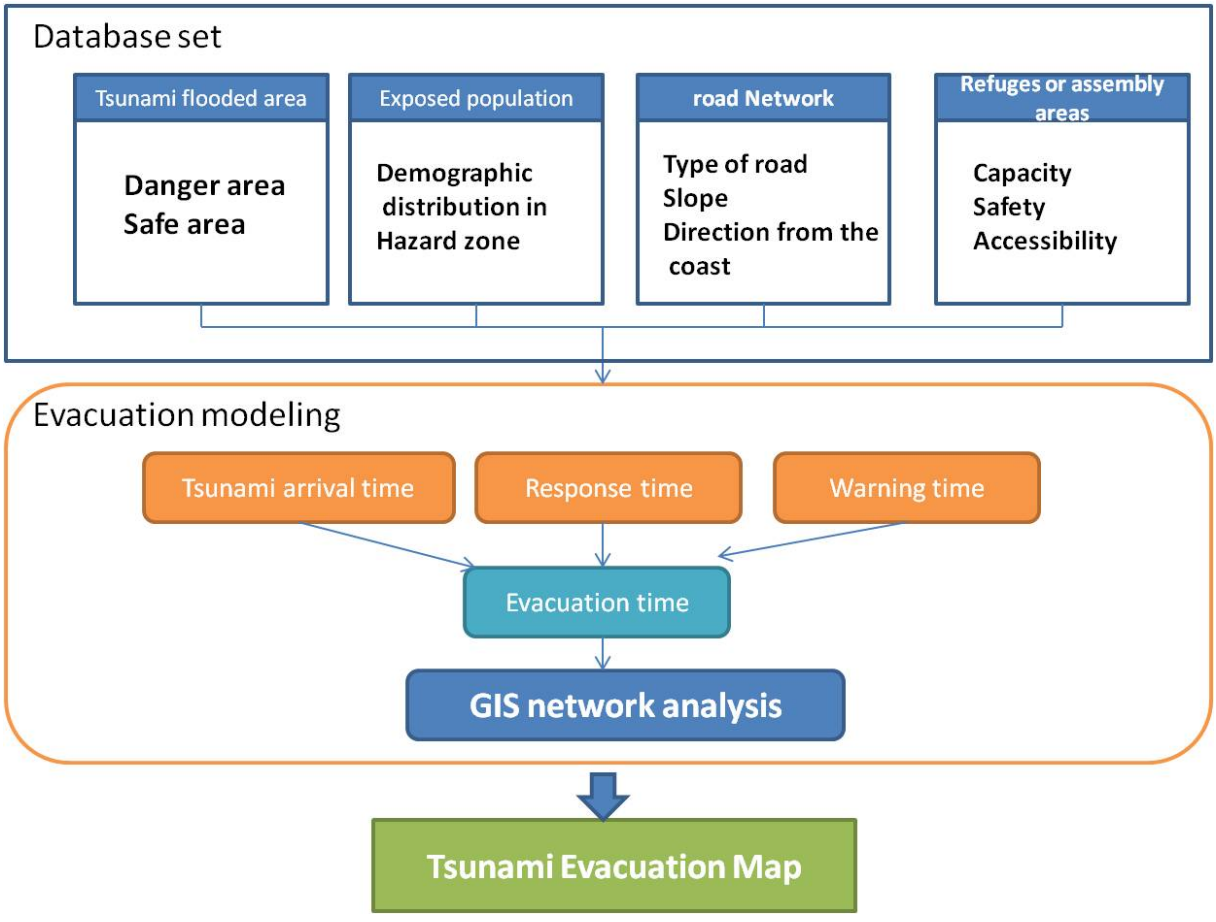

Figure 2: Flow chart indicating the methodology adopted for this study

4. STUDY AREA

The city of Tangier is located in the northern coast of Morocco with a population circa 948.000 according to population census of 2014. It lies at the western entrance to the Strait of Gibraltar where the Mediterranean meets the Atlantic Ocean (Fig. 3A). Its coastal zone covers an area of about 15 km long from west to the east. The city is knowing rapid development and modernization. the port city includes new tourism projects with many hotels and modern business centers. Tangier economy depends in general on tourism with nice beaches like Municipal, Malabata and Ghandouri beach (Fig. 3B), pedestrian avenues and terraces ranging front of the bay. The crowded beaches specially during summer months and the several seaside resorts increase the population exposure in Tangier city to tsunami threat. Until now this city doesn't has an official tsunami evacuation plan, this work could help emergency planners to adopt some evacuation routes after being validated.

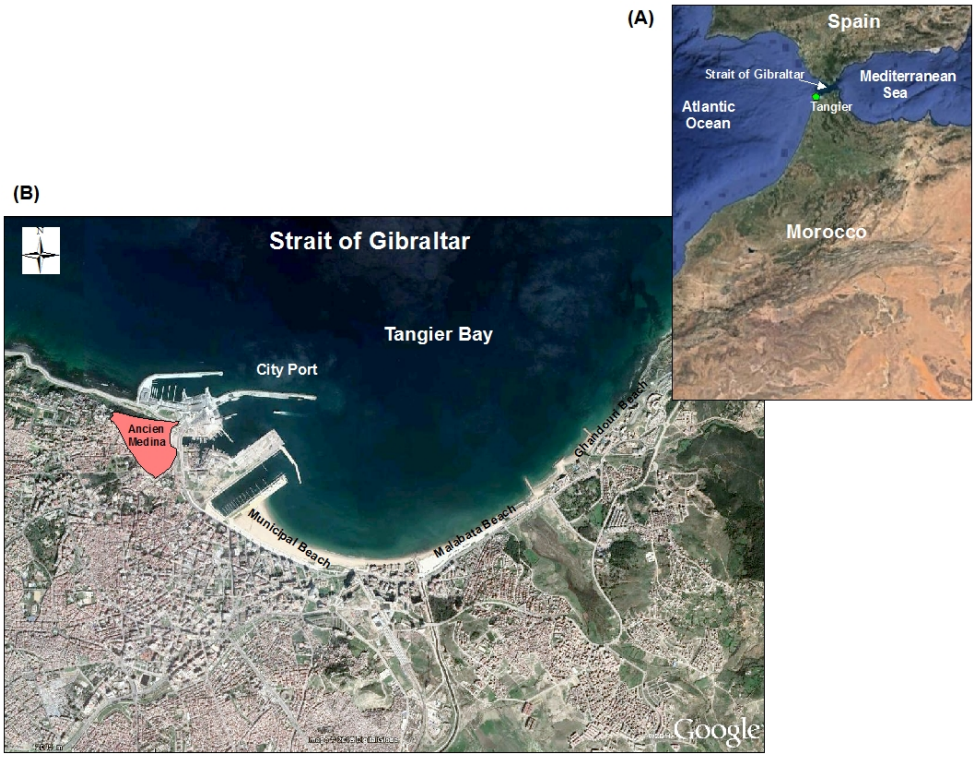

Figure 3. Study area: (A) regional overview (B) Tangier map with principal locations as the city port, the ancient Medina and the important beaches.

4.1 EVACUATION AREA OR DANGER ZONE

The evacuation area corresponds to the expected extension of the flooding in land. The inundated area in Tangier is drawn based on deterministic approach, considering tsunami threat from the tsunamigenic sources located in the SW Iberian Margin. Modeling was applied for different scenarios based on the Most Credible Earthquake Scenarios (Tinti and Armigliato 2003), details of the sources are defined in ASTARTE-D8.8 (2015) (http://www.astarte-project.eu). The Cadiz Wedge Fault (CWF) with Mw=8.75 is considered the worst credible earthquake scenario, able to cause the higher impact tsunami for Tangier. The inundation map (Fig. 4) shows that over 6.2 km^2 of the coastal area is prone to inundation with maximum flow depths range from 0.1m to 10m. The highest inundation distances are mostly calculated in flat areas specialty along the rivers where the horizontal inundation exceeds 2.7 km. This penetration is due mainly to the low topography of these areas. This map shows also that horizontal inundation doesn't exceed 60 m from the shoreline at its east and west side due to the high topography of the hills that exceed generally 20 meters. The estimated inundated area is considered as danger zone', therefore all non-inundated zones could be considered as safe zones.

4.2 ESTIMATION OF THE EXPOSED POPULATION

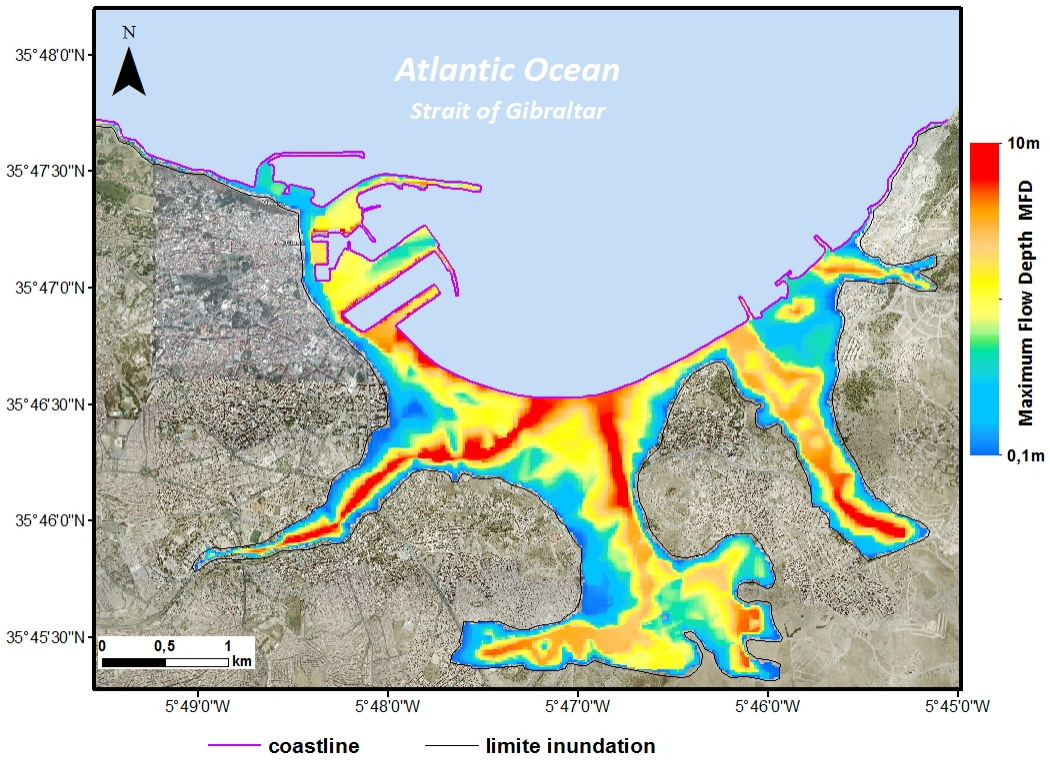

Figure 4: Inundation zone map for Tangier, simulation was based on the Cadiz Wedge fault source (ASTARTE-D8.8, 2015, http://www.astarte-project.eu)

To carry out the evacuation routes modeling, it is necessary to know the number of people (residents or not) located in the potential tsunami inundation zone and their distribution. For Tangier city, demographic data was provided by the institution "Haut Commissariat au Plan, HCP" collected during the general population census in 2014. This data provides a spatial distribution of the population by each district. Along the hazard zone, there are 63 districts divided in three communes (Fig. 5); Tangier-Medina, Charf-Souani and Charf-Mghogha. The Charf-Mghogha commune is the most populated with about 10000 residents, followed by Tangier-Medina commune with an estimated population of 3200. The Charf-Souani commune is the less populated with about 900 residents.For more complete database, and due to lack of official information related to the number of tourist visiting the beaches on high seasons, we added 3000 people (estimation of civil protection officer in Tangier) assumed as temporarily residents coming for work from outside of the hazard zone. They are supposed located, during the day and out of the high touristic season (summer), along the cornice and at the beaches (Municipal, Malabata and Ghandouri beaches, Fig. 3B). In total, the estimated population at the inundated area correspond to about 17100 people.

Ideally, people evacuate from each building block and try to take the shortest way to reach safe areas. In order to estimate the number of people to evacuate in each building block, we need demographic attributes at each residence. Due to the deficiency of these data, we start the modeling from the center of each district where evacuees are expressed in term of points. We note that, we ignored the different situations of evacuees (location inside or outside of buildings, activities, ...) since we used macro-simulator approach.

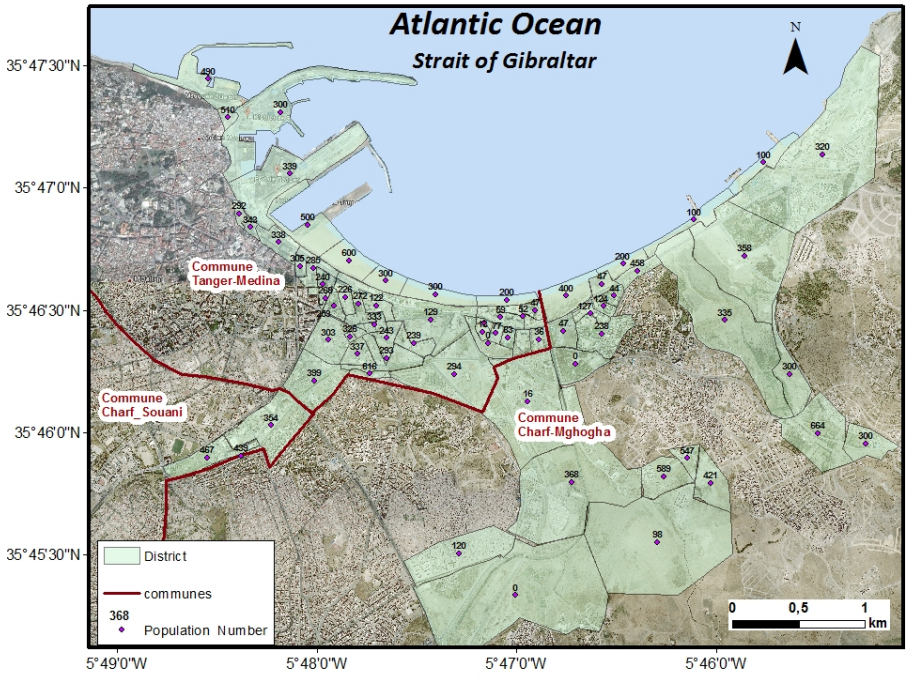

Figure 5: Spatial distribution of the population by district in Tangier flooded areas

4.3 ROAD NETWORK

Detailed road network is necessary to be implemented in the network modeling. We achieved a road network for coastal zone of Tangier which shows main roads that could be used as escape routes in case of tsunami (see Fig. 6).

Roads were digitized in Arc GIS from high resolution (40 cm) orthophotos (2009). In order to have more detailed road networks, missing roads were digitized from recent Google Earth images. The attributes related to the dataset network include for each path; name of major streets, length, capacity (width), traffic direction, restricted turns and special descriptions. Finally, the elaborated road network includes 1624 paths with 948 network connectivity (nodes).

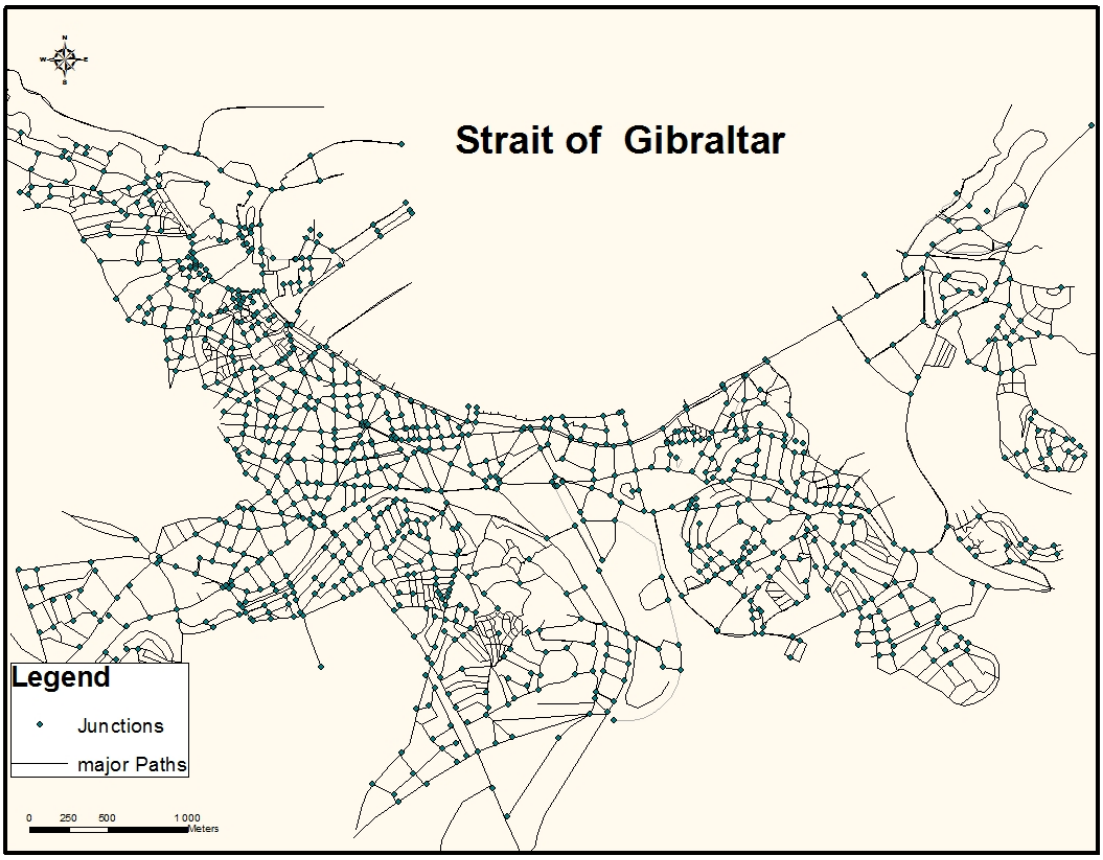

Figure 6: Road network in Tangier flooded zone

4.4 EVACUATION SHELTER BUILDINGS

Tsunami is an event who has long period to be occurred in Morocco, so, there are no buildings functioning specially as evacuation shelter buildings in Tangier. In this study, we tried to find suitable assembly areas or evacuation buildings shelters responding to different criteria such as location, accessibility, known by the population and capacity.
First, we identified several evacuation shelters buildings and assembly areas from recent Google Earth images, then we conducted a field survey to validate or exclude the identified sites. We finally retained 15 sites located not far to the inundated area, have easy access through the existing road network and are able to accommodate a large number of evacuees. Figure 7 illustrates the distribution of buildings shelters and assembly areas along the study zone.

Figure 7: Map indicating the location of evacuation shelters buildings/ assembly areas with some photos

These sites corresponds to: i) evacuation shelters buildings; as Mosques (Grande Mosque, Mosque Assouriyine) or schools (Moulay Youssef school, Roi Fahd school and Sakia El Hamra school). They are able to shelter the evacuees for a considerable period since they have appropriate infrastructures (rooms, drinking water, electricity...) and ii) assembly areas like; public gardens (United Nations garden, Tanja Al Balia garden) or high

topography areas (forest or bare land), these areas could accommodate evacuees temporarily. The total capacity of the proposed refuge sites seems to be sufficient in case of a real threat because it exceeds 17100 people estimation. The proposed assembly areas or evacuation building shelters should be validated by the local authorities before adopting an official evacuation map.

5. TSUNAMI EVACUATION MODELING

The principal action of an evacuation is to ensure that, in case of risk, people move from a relatively danger zone to safer places via routes that are free from significant danger. Furthermore, the main goal of evacuation is to save lives.

NTHMP (2001) explained that there are two methods to evacuate people from tsunami hazard zones; a) Horizontal evacuation; when evacuees move from the hazard zones to the safer areas or higher grounds (hills) located out of the inundation area; b) Vertical evacuation; when threatened community evacuate to nearby higher floors of tsunami resistant buildings. Vertical evacuation is needed for near-source generated tsunamis which there is not enough time between warning and the arrival of the first tsunami wave.
To achieve a good modeling of evacuation routes some parameters should be taking account.

5.1 SPEED OF EVACUEES

According to the Intergovernmental Oceanographic Commission report (IOC, 2008); to ensure safe evacuation, several risk management programs prohibit residents to evacuate by their personal vehicles for all types of disasters. In the case of a local tsunami where the source is close to the coastal zones, the waves could arrive in 30 minutes or less after the trigger of the earthquake. Threatened persons are encouraged to walk to safe areas because in such cases, the use of vehicles can not only block the roads but constitute a real menace to people life.

In this study, evacuation was assumed to be performed by walking. As the network analysis is based on time traveling, we have defined two more parameters; the speed of pedestrians and topography (slope). These parameters are considered able to influence the movement of evacuees along the routes before reaching the selected safe areas.

Pedestrians speed was identified from available bibliographic references. Dewi (2012) used for modeling evacuation routes in the coastal area of Cilacap (Java, Indonesia), the walking speed equal to 0.751 m/s. To model the behavior of persons in Arahama locality (District Miyagi, Japan) during the evacuation, Mas et al (2012) suggested an average speed of 1.1 m/s and a maximum speed of 1.33m/s. Scheer et al. (2012) consider an average human speed of 1 m/s while in ground where it is difficult to move as beaches, a speed of 0.5 m/s is proposed. Gonzalez Riancho et al. (2013), considered for modeling the evacuation in the

coastal area of El Salvador, two types of pedestrian velocity; the rapid one 1m/s for adults and the slow one 0.7m/s for children, elder, and disabled people . A "comfortable" pedestrian speed without interaction with other people or with physical barriers of 1.3 m/s was adopted by Sahal et al (2013) and applied to pedestrians evacuation at Côte d'Azur (France).

According to these different studies, the proposed pedestrian speed vary from 0.5 m/s to 1.33 m/s. In this work and since we don't know the pedestrian velocity for people living in Tangier, we adopted an average speed, therefore, the value of pedestrian speed taken is 1.03 m/s.

Tangier is a city with many slopes, we assume that this situation will decelerate the evacuation, that why a correction of walking speed based on the slope is necessary. To calculate the slopes from the DEM (10m) used in tsunami modeling, we took in account the difference in altitude between the lowest points considered as origins and the high points considered as destinations. New values of pedestrian speed were calculated on the basis of the coefficients reduction proposed by Laghi et al. (2006, see Table1). The road network has been divided into 16 classes of slopes extracted from DEM with a range of 3%, we obtained 16 classes of corrected speeds values varying from 1.03 m/s to 0.10m/s.

5.2 ESTIMATED TSUNAMI ARRIVAL TIME (ETAT)

The Estimated Tsunami Arrival Time (ETAT) is the time required for the first tsunami wave to travel from its source to a certain point in the coast (IOC, 2008). It is defined as the time that elapsed between the end of the earthquake and the arrival onshore of the first wave of the tsunami.

The estimated tsunami arrival time may vary from minutes to several hours depending on the type of tsunami which can be local, regional or transgenic. The first wave of local tsunami may hit the coastal area in a few minutes after the earthquake and can have important damage to coastal areas. On the other hand, distant tsunamis can travel for hours before striking coastal areas. The type of tsunami will determine the time required to alert the population in order to evacuate.

To simulate arrival time of the first tsunami wave to reach the Moroccan coasts, we used the TTT (Tsunami Travel Times). The TTT maps are obtained using TTT software (figure 8), this program calculates the first arrival travel times with global bathymetry grids for a tsunami generated in a given source. For Tangier, calculation was based on two tsunami scenarios, the Horseshoe fault (HSF) and the Cadiz Wedge fault (CWF), details of the sources are given in ASTARTE-D8.8 (2015) (http://www.astarte-project.eu).

Results showed that the first wave of the tsunami will reach the Tangier coastal area in 0.9 hour (54 minutes) for the HSF scenario and in 0.8 hours (48 minutes) for the CWF scenario. As we are interested of the worst case scenario, we considered the shortest time of

48 minutes corresponding to the estimated tsunami arrival time. This time gives an idea to the available time for the threatened population to evacuate tsunami hazard zones.

Table 1: Evacuation speed correction based on the slope (Laghi et al., 2006).

Slope	Speed value	Slope	Speed value
0 - 3	100%	***24-27***	25%
3-6	85%	***27-30***	20%
6-9	70%	***30-33***	15%
9-12	55%	***33-36***	14%
12-15	45%	***36-39***	13%
12-18	40%	***39-42***	12%

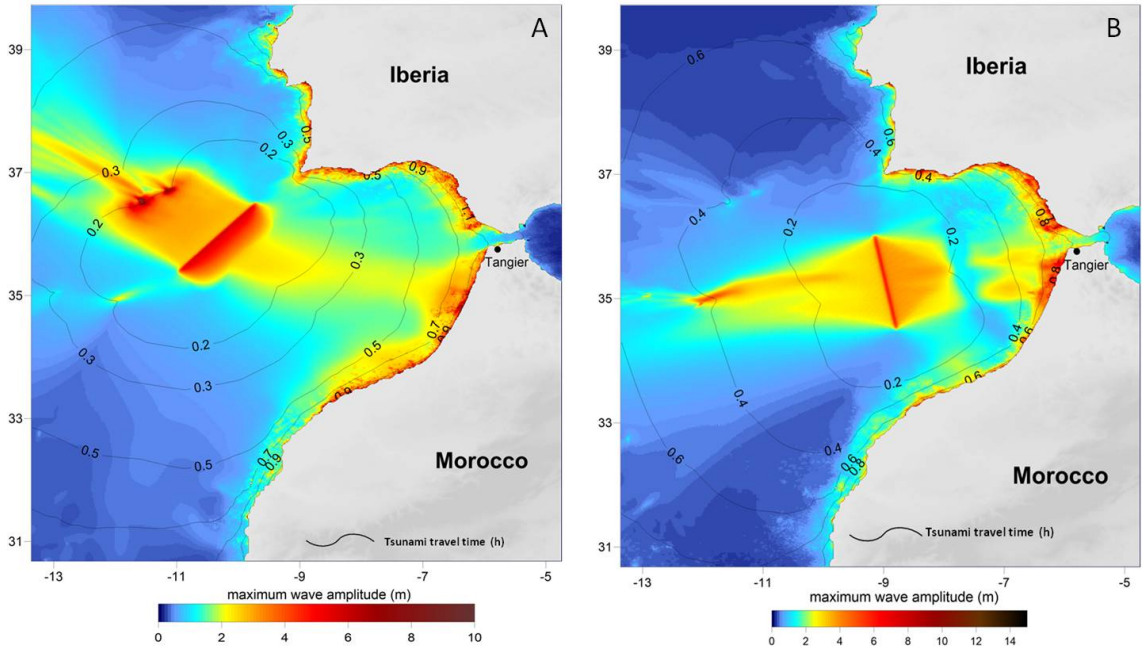

Figure 8: Simulation of the first tsunami arrival time to Moroccan coasts using TTT software for two tsunami scenarios, A) the Horseshoe fault (HSF) and B) the Cadiz Wedge fault (CWF).

5.3 EVACUATION TIME (ET)

Evacuation Time (ET) is the time that the alerted population need to reach a secure area (refuge site) before the first tsunami wave arrive. The evacuation time can vary according to the type of tsunami from several minutes to hours. In order to define the evacuation time (ET) for Tangier, we used the formulae proposed by Dewi (2012):

$$ET = ETAT - WT - RT$$

ETAT: Estimated Tsunami Arrival Time (48mn)
WT: Warning Time
RT: Response Time of the population

Warning Time (WT) is defined as the time required to tsunami warning center to take the decision to disseminate the information to the authority. Generally, a threatened community is considered timely warning when the alert time is less than 15 min. For our study, we considered the warning time proposed by Omira et al. (2009). These authors suggested that for ensuring the best evacuation for the city of Tangier, the minimum warning time should be between 20 and 30 minutes. In our study, we decided to take an average value of 25minutes as Warning Time (WT).

-

Response Time (RT) of evacuees depends on the degree of awareness of the threatened population. It's preferable that people leave the danger area immediately after an official warning. However, in most of time , people don't evacuate even the authorities suggest to do it. Mas et al. (2012) reported that the survey conducted in Miyagi, Iwate and Fukushima after the Tohoku-Oki tsunami and which concerned 870 survivors, showed that only 57% have evacuated immediately after the earthquake and 37% have taken more time to evacuate. Suppasri et al.(2013) reported that a survey accomplished after the same tsunami in Kamaishi and Natori cities (Japan) shows that 60% of 113 interviewees in Kamaishi evacuated less than 10 minutes while in Natori only 30% of 105 interviewees evacuated between 20 and 30 minutes. For Tangier, the population response time is supposed to be 10 minutes, it it's an optimistic estimate due to the low level of awareness of Tangier population.

After given values to the three factors that seem influence the evacuation time (ET) which are; the estimated tsunami arrival time (48 minutes), the warning time (25 minutes) and population response time (10 minutes), the calculated evacuation time (ET) is 13 minutes.

6. RESULTS AND DISCUSSION

In this study, we used the Closest Facility tool to obtain the most efficient time to go to the nearest evacuation shelter points. While solving the analysis, restrictions attributes including capacity limits of the paths or high degrees of the slope were chosen to prohibit some evacuees to traverse certain roads in order to avoid pedestrian congestion.

After solving the routes, the results are displayed in a graphic layers map. Figure 9 demonstrates an evacuation plan with the position of horizontal shelters and assembly areas. The areas to evacuate (danger) are displayed in blue color whereas the refuge zones (safe) in green, the evacuation roads are represented in different colors according to the calculated evacuation travel time.

Modeling results suggest that the total of the study area could be evacuated in less than 25min. The minimum time modeled for evacuation is 3.05 min whereas the maximum time needed to be in a safe place is 25 min. Also the capacity of the proposed shelters seems to be sufficient because at the end of the modeling all the threatened population have reached the safe areas.

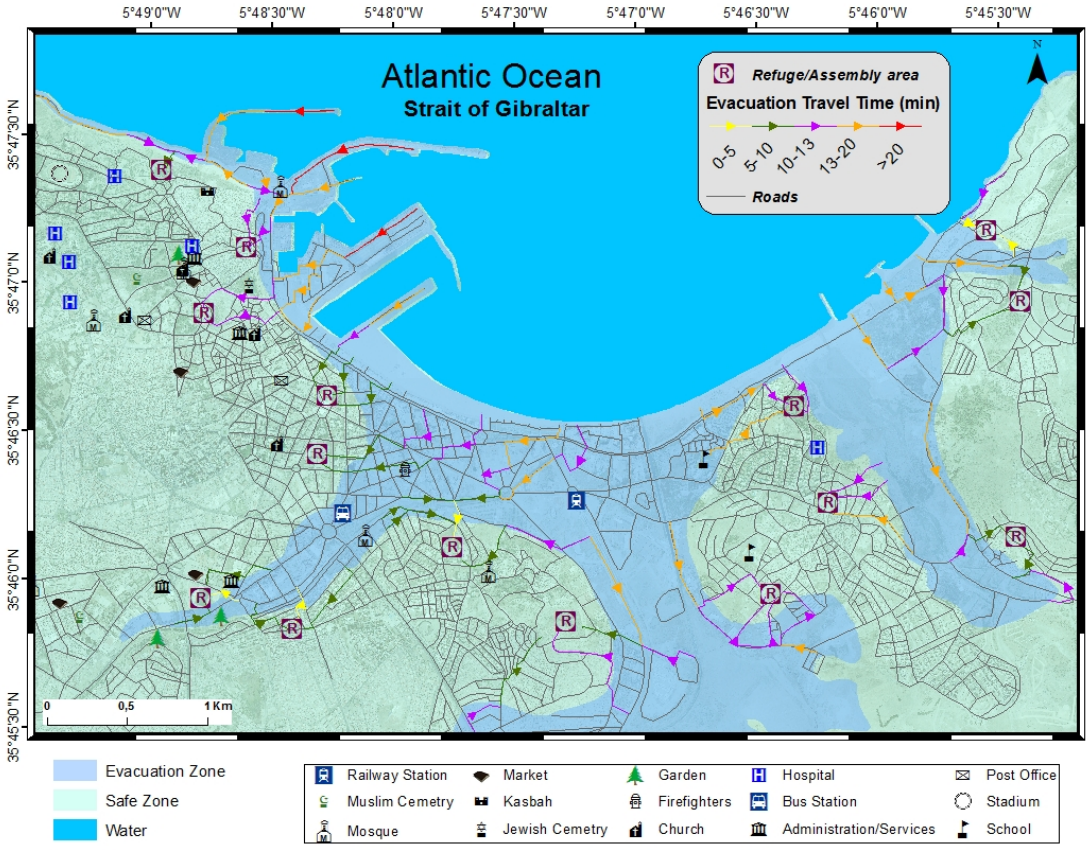

Figure 9: The proposed tsunami evacuation plan for Tangier city.

The results suggested that nearly 72% of the threatened population (12312 evacuees) could be sheltered in less than the calculated Evacuation Time ET (13 min). The remaining population (4788 evacuees) with evacuation travel time larger than 13 min are susceptible to the coming tsunami waves. For this part of the community, vertical evacuation refuges or shelters in the flooded area could be proposed for hosting temporarily these evacuees.
Also, if we want to have more time to evacuate, it is necessary that population react properly in a short of time. Awareness campaigns, distribution of brochures and training exercises are very useful to increase community resilience. These actions permit to explain to the potentially affected population the best attitude to take in case of tsunami warning

and when an earthquake is felt, threatened people should immediately evacuate to high areas or vertical shelters without waiting for an official warning from local authorities.

7. CONCLUSIONS

This study proposed a tsunami evacuation plan for the city of Tangier-Morocco. Evacuation modeling based on GIS tools was applied to find the most effective routes taking into account the shortest travel time to evacuate hazard zones in case of tsunami during the low season. Modeling was achieved using detailed input data of road network, evacuation building shelters or assembly areas and spatial distribution of the population in the hazard zone. Results are presented in an evacuation plan in which the escape routes, safe locations and assembly points are clearly marked. The proposed map need to be validated by local authorities and emergency planners in order to produce an official evacuation plan for Tangier city.

Many advances could be carried out in future studies; detailed data of the local population will help to consider building blocks as origin points for modeling. This will make the model more realistic since it represents the real condition where people start moving from. We recommend for next works, to take into account the high variation of daily or seasonal touristic fluctuations; several evacuation scenarios could be implemented by varying the number of population (day/night, high/low season) or the profiles of people (adults, children, and disabled).

ACKNOWLEDGEMENTS

This work is funded from collaborative project ASTARTE - Assessment Strategy and Risk Reduction for Tsunamis in Europe Grant 603839, FP7. Our gratitude is also addressed to the reviewers for taking time to review this paper.

REFERENCES

CRATER program (2005) "Coastal Risk Analysis of Tsunamis and Environmental Remediation ". Evacuation routes tools ArcGIS® toolbox**,** user's manual, 88p.

Dewi, R.S. (2012). A-Gis Based Approach of an Evacuation Model for Tsunami Risk Reduction. Journal of Integrated Disaster Risk Management. DOI10.5595/idrim.2012.0023.

FEMA (2009).Vertical Evacuation from Tsunamis. A Guide for Community Officials. Federal Emergency Management Agency, National Earthquake Hazard Reduction Program . P646A / June 2009.

González-Riancho, P., Aguirre-Ayerbe, I., Aniel-Quiroga, I., Abad, S., González, M., Larreynaga, J. et al. (2013). Tsunami evacuation modeling as a tool for risk reduction: application to the coastal area of El Salvador Nat. Hazards Earth Syst. Sci., 13, 3249–3270, 2013. doi:10.5194/nhess-13-3249-2013.

Hamacher, H.W., and Tjandra, S.A. (2001). Mathematical Modeling of Evacuation Problems: A State of Art, Berichte des Fraunhofer ITWM, n° 24, 45p.

Helbing, D., and Molnar, P. (1995). Social force model for pedestrian dynamics. Physical Review E, vol.51, n°5.

Intergovernmental Oceanographic Commission IOC (2008). Tsunami preparedness information guide for disaster planners. Manuals and Guides. UNESCO, n°49, p29.

Klüpfel, H., Meyer-König, T., Wahle, J., and Schreckenberg, M. (2000). Microscopic simulation of evacuation processes on passenger ships, In: Proceedings ACRI 2000, vol. 2000, pp. 63-71.

Laghi, M., Cavalletti, A., and Polo, P. (2006). Coastal risk analysis of tsunamis and environmental remediation, Asian Disaster Preparedness Center, Klong Luang, Thailand, 98 pp., 2006.

Lammel, G., Hubert Klupfel, H., and Nagel, K. (2008). Preliminary Result of a Large Scale Microscopic Evacuation Simulation for the City of Padang in the Case of Tsunami, Pedestrian and Evacuation Dynamics. Proceedings of the 4th international conference, Wuppertal, 2008. Springer, Berlin.

Leone, F., Péroche, M., Lagahé, E., Gherardi, M., Sahal, A., Vinet, F., and al. (2013). Modélisation de l'accessibilité territoriale pour l'aide à la gestion de crise tsunami (Mayotte, France), Annales de Géographie, Ed. A. Colin, Paris, No. 693, 502–524.

Mas, E., Imamura, F. and Koshimura, S. (2012). An agent based model for the tsunami evacuation simulation. A case study of the 2011 great east Japan tsunami in Arahama town. 9th International Conference on Urban Earthquake Engineering/ 4th Asia Conference on Earthquake Engineering March 6-8, 2012, Tokyo Institute of Technology, Tokyo, Japan.

Nagel, K., and Schreckenberg, M. (1992). A cellular automaton model for freeway traffic. Journal de Physique I, vol. 2, n°12, pp.2221-2229. http://dx.doi.org/10.1051/jp1:1992277.

NTHMP (2001) "National Tsunami Hazard Mitigation Program". Designing for tsunami. Seven principles for planning and designing for tsunami hazards. USA, NOAA, USGS, FEMA, NSF, Alaska, California, Hawaii, Oregon and Washington.

Omira, R., Baptista, M.A., Matias, L., Miranda, J.M., Catita, C., Carrilho, F., and Toto, E. (2009). Design of a Sea-level Tsunami Detection Network for the Gulf of Cadiz. Nat Hazards Earth Syst. Sci. 9:1327–1338. doi:10.5194.

Pararas-Carayannis, G., 1997. The Great Lisbon Eartrhquake and Tsunami of 1 November 1755. http://www.drgeorgepc.com/Tsunami1755Lisbon.html

Pararas-Carayannis, G., 2011.TSUNAMIGENIC SOURCE MECHANISM AND EFFICIENCY OF THE MARCH 11, 2011 SANRIKU EARTHQUAKE IN JAPAN, Science of Tsunami Hazards, Vol. 30, Number 2, 2011.

Pararas-Carayannis, G., 2011a. The Great Tsunami of March 11, 2011 in Japan - Analysis of Source Mechanism and Tsunamigenic Efficiency. OCEANS 11, MTS/IEEE Proceedings, 2011

Pararas-Carayannis, G., 2011b. Earthquake and Tsunami of 11 March 2011 in Sanriku, Japan http://www.drgeorgepc.com/Tsunami2011JapanSanriku.html

Pararas-Carayannis, G., 2014, The Great Tohoku-Oki Earthquake and Tsunami of March 11, 2011 in Japan: A Critical Review and Evaluation of the Tsunami Source Mechanism. Pure and Applied Geophysics, December 2014, vol 171, Issue 12, pp 3257-3278.

Péroche, M., F., Leone, and Gutton, R. (2014). An accessibility graph-based model to optimize tsunami evacuation sites and routes in Martinique, France, Advances in Geosciences, 38, 1-8, doi:10.5194/adgeo-38-1-2014.

Pidd, M., De Silva F.N., and Eglese, R.W. (1996). A simulation model for emergency evacuation. European Journal Of Operational Research, 1996, vol. 90, pp. 413-419.

Sahal, A., Leone, F., and Péroche, M. (2013). Complementary methods to plan pedestrian evacuation of the French Riviera's beaches in case of tsunami threat: graph- and multi-agent-based modeling - Nat. Hazards Earth Syst. Sci., 13, 1735–1743. doi:10.5194/nhess-13-1735-2013.

Shahabi, K., and Wilson, J.P. (2014). CASPER: Intelligent capacity-aware evacuation routing. Computers, Environment and Urban Systems, vol. 46, pp. 12–24.

Saito, T., and Kagami, H. (2004). Simulation of evacuation behavior from tsunami utilizing multi agent system. 13th World Conference on Earthquake Engineering Vancouver, B.C., Canada August 1-6, 2004 Paper No.612.

Scheer, S.J., Varela, V., and Eftychidis, G. (2012). A generic framework for tsunami evacuation planning. Physics and Chemistry of the Earth 49 (2012), pp. 79–91.

Steiner, A., Philipp, M. and Schmid, A., (2007). Parameter Estimation for a Pedestrian Simulation Model, in actes du colloque "7th Swiss Transport Research Conference". Ascona, Switzerland.

Suppasri, A., Mas, E., Koshimura, S., Charvet, I., Gunasekera, R., Imai, K., and al.(2013). Building damage characteristics based on surveyed data and fragility curves of the 2011 Great East Japan tsunami. Nat Hazards 66:319–341.

Tinti, S., Armigliato, A. (2003). The use of scenarios to evaluate the tsunami impact in southern Italy. Marine Geology. 199: 221-243.

Wood, N., Jones, J., Schmidtlein, M., Schelling, J., and Frazier, T. (2016): Pedestrian flow-path modeling to support tsunami evacuation and disaster relief planning in the U.S. Pacific Northwest International Journal of Disaster Risk Reduction. Volume 18, September 2016, pp 41-55.

ISSN 8755-6839

SCIENCE OF **TSUNAMI HAZARDS**

Journal of Tsunami Society International

Volume 37 **Number 4** **2018**

CHARACTERISTICS OF THE TSUNAMI WAVE REFLECTION FROM THE BEACH

R.Kh. Mazova[1], I.V. Remizov[1], N.A. Baranova[1], Yu.F. Orlov[1], S.M. Nikulin[1], A.V. Andriyanov[1], V.D. Kuzin[1]

[1]Nizhny Novgorod State Technical University n.a. R.E. Alekseev, Nizhny Novgorod, RUSSIA

ABSTRACT

It is well known that reflection from the complex relief of the continental slope can significantly affect the runup of a long wave on the beach and significantly increase the destructive impact on the coast. In this paper, we consider the reflection of long waves from a plane slope and from a slope conjugated with even bottom. The problem is considered both for a monochromatic wave and for an arbitrary initial perturbation. Using the "vertical wall" and "plane slope" approximations, the reflection coefficients and the solution for the reflected wave are obtained. Numerical simulation is carried out for the case of reflection of the "Lorentz pulse" from the slope, which is conjugated with even bottom. The results obtained are in good agreement with the available results, both an analytical study of the process and numerical modeling of runup of an arbitrary initial perturbation with taking into account of reflection from the shore.

Keywords: *long gravitational wave, reflection wave from the beach, analytical solution, reflection coefficient, reflection of the pulse of arbitrary form.*

Vol 37. No. 4, page 175 (2018)

1. INTRODUCTION

The study of the characteristics of the long gravitational wave (tsunami) reflected from the beach is interesting not only for a more complete understanding of the processes taking place in the coastal zone during the wave runup, but also for solution specific tasks of coastal engineering. The main point in coastal engineering is to understand the coastal behavior of wave movements: in particular, to assess both the maximum runup in abnormally large waves on the beach, and the problems of water withdrawal from the shore.

It is well known [Belokon, Semkin, 1998] that reflection from the continental slope and other irregularities of the bottom relief in many cases can significantly affect the runup of the long wave and their destructive impact on the coast. In general, the coastal relief is quite complex, so the problem of reflection is solved approximately. However, often large inhomogeneities such as an underwater ridge or a continental slope are elongated along one of the directions, what makes it possible to simplify the formulation of the problem. One of the important issues that makes it possible to solve the problem of wave reflection from the shore is the task of interpretation of a record of a tide gauge in the coastal zone that records a complex superposition of incident, reflected, and diffracted waves [Volzinger et al., 1989]. The coefficients of wave reflection from the underwater slope as well as from a plane slope were considered in a number of works (see, for example, [Kozlov, 1981, Pelinovsky, 1982, Mazova, 1984]). The problem of reflection of long sea waves from flat slopes and slopes conjugated with even bottom has also been many times considered in the literature [Sugimoto, Kakutani, 1984, 1988; Synolakis, 1987; Jeffrey, Day, 1988, 1989; Day, Jeffrey, 1989].

2. STATEMENT OF THE PROBLEM

After the wave climbed the bench, the rundown process begins and a reflected wave is generated that propagates to the sea. As shown in [Sugimoto, Kakutani, 1988], a reflected wave can be observed only at distances from the shore $x > 2.5d$, where d is the depth of water above a flat bottom. Close to the shoreline, at $x < 2.5d$, the incident and reflected waves can not be differentiated - they merge into one wave. The reflected wave has a dipole character, and although both the linear and nonlinear theories predict perfect reflection for non-breaking waves, the dipole nature of the reflected wave is clearly expressed. Because linear and nonlinear theories are in good agreement with laboratory data at the base of the coast, apparently, the dipole wave is transformed into a wave of one sign only after passing over a region of constant depth. The results of numerical modeling of wave reflection from a vertical wall lead to similar conclusions [Zheleznyak, 1985]: when reflected from a wall, the wave at small distances is essentially asymmetrical and a pronounced trough follows the crest. Over time, the waveform is approaching the original, but complete recovery does not occur - behind the single wave it is a train and an oscillating "tail". Analogous phenomena are observed at high-amplitude waves in laboratory experiments (see Zheleznyak, 1985). Very long waves "see" the shore as a vertical wall: the wavelength changes rapidly and the reflection appears immediately. Shorter, steeper waves, at first, at

least, go ashore, as if there would be no shore. The wavelength remains constant and the reflection begins only when the total wave has come ashore [Synolakis, 1987].

When unbroken waves run to the shore, the reflected wave is generated continuously, this reflection is manifested as a "trail" between incoming and outgoing waves. However, the magnitude of the reflected wave, generated at a wave height in the open ocean of $H = 0.3d$, is negligible, until the wave reaches the maximum runup and the reflection process begins [Synolakis, 1987]. The process of reflection from a sloping beach is usually characterized by a reflection coefficient, which is the ratio of the incident and reflected waves. Because the height of the reflected wave can not be determined exactly due to the dipole nature of the wave, it is possible to determine the reflection coefficient from the ratio of the height of the positive dipole wave to the height of the incident wave [Synolakis, 1987].

2. REFLECTED WAVE FROM A PLANE SLOPE

It is obvious that the problem of reflection of a long wave from the shore is solved in direct connection with the problem of wave runup onto a slope. In the works [Mazova, Pelinovsky, 1982; Mazova 1984], the problems of runup in the framework of a linear and nonlinear formulation of the problem were considered in neglecting dispersion and dissipation. In this case, the nonlinear equations of shallow water by means of the Carrier-Greenspan transformations are reduced to a linear equation for the elevation of the water surface [Pelinovsry, 1982; Sugimoto and Kakutani, 1984; Sugimoto and Kakutani, 1988; Synolakis 1987; Jeffrey and.Dai 1988; Dai and A.Jeffrey 1989; Zheleznyak 1982; Mazova and Pelinovsky, 1982; Mazova et al, 1982].
The linear wave equation is solved

$$\frac{\partial^2 \eta}{\partial t^2} - g\frac{\partial}{\partial x}(h(x)\frac{\partial \eta}{\partial x}) = 0, \tag{1}$$

Then the solution for a monochromatic wave runup in the "classical" geometry: the plane slope $h = -\alpha x$, the wave moves along the normal to the shore, gives the wave field as the sum of the fields of the incoming and reflected waves (Fig. 1) (see, for example, [Mazova , 1984])

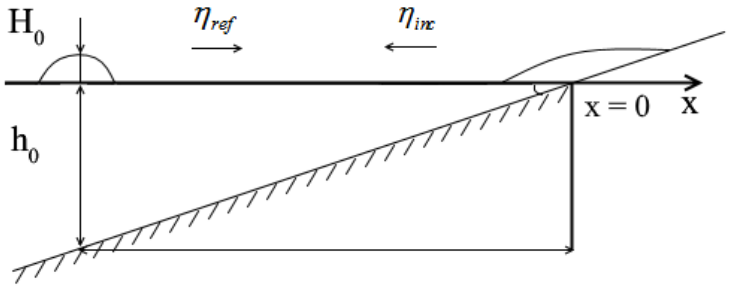

Fig. 1. The geometry of the problem for a plane slope.

$$\eta(x,t) = a(x)\left\{\sin\left[\omega\left(t - \int\frac{dx}{\sqrt{gh(x)}}\right) - \frac{\pi}{4}\right] + \sin\left[\omega\left(t + \int\frac{dx}{\sqrt{gh(x)}}\right)\right]\right\}, \quad (2)$$

where $a(x) = \frac{A}{2}\left[\frac{g\alpha^2}{\pi\omega^2 h(x)}\right]$; $t = \mp\int\frac{dx}{\sqrt{gh(x)}}$ is the time of wave movement from isobath h_0 to the shoreline (-) and back (+).

Those solution in the most general form is a superposition of two waves with a frequency ω and with a variable amplitude a (x). The coefficient A can be found by taking the amplitude of the incident wave at the depth h_0 to be equal H_0. Then we will have

$$\eta(x) = 2\pi H_0\sqrt{\frac{2L_0}{2\pi\sqrt{gh_0}}}\sqrt{\omega}J_0\left(4\pi\sqrt{\frac{L_0\,|\,x\,|}{\lambda_0}}\right), \quad (3)$$

where L_0 is the shelf length, λ_0 is the wavelength at isobath h_0, J_0 is the Bessel function.

The solution for runup of pulse wave can be obtained applying the Fourier superposition of solutions like (2), considering $H_0 = H(\omega)$

$$\eta(x,t)_{\pm} = 2\left(\frac{\pi}{\alpha}\right)^{\frac{1}{2}}\left(\frac{h_0}{g}\right)^{\frac{1}{4}}\int_{-\infty}^{\infty}\sqrt{|\,\omega\,|}\,\mathrm{sgn}\,\omega H(\omega)J_0\left(\omega\sqrt{\frac{4\,|\,x\,|}{g\alpha}}\right)e^{i\omega t}d\omega, \quad (4)$$

or, in the form more convenient for further transformations [Mazova, 1984; Voltsinger et al., 1989]

$$\eta(x,t)_{\pm} = \frac{-i\,\mathrm{sign}\omega}{\sqrt{\pi g\alpha\sqrt{gh}}}\int_{-\infty}^{\infty}\sqrt{|\,\omega\,|}\,\mathrm{sgn}\,\omega H(\omega)e^{i\omega\left(t\mp\int\frac{dx}{\sqrt{gh(x)}}\right)-\frac{\pi}{4}\mathrm{sign}\omega}d\omega, \quad (5)$$

where $H(\omega)$ is the spectrum of a coming wave. This solution also consists of the sum for the fields of the incident and reflected waves. Knowing the shape of the incident wave at a depth h_0, we can calculate its spectrum

$$H(\omega) = \frac{-ig\sqrt{g\alpha\sqrt{gh_0}}}{2\sqrt{\pi}}\frac{1}{\sqrt{|\,\omega\,|}}\mathrm{sgn}\,\omega\cdot e^{-i\frac{\pi}{4}\mathrm{sgn}\,\omega}\int_{-\infty}^{\infty}\eta_+(t')e^{-i\omega t'}dt'. \quad (6)$$

Submitting (6) to (5) we have

$$\eta_{\pm}(x,t) = \frac{-i}{\pi}\mathrm{sgn}\,\omega\int_{-\infty}^{\infty}e^{i\omega\left(t\mp\int\frac{dx}{\sqrt{gh(x)}}\right)}d\omega\int_{-\infty}^{\infty}\eta_+(t)e^{-i\omega t'}dt'. \quad (7)$$

From formulas (2) and (5) it can be seen that the amplitude of the reflected signal does not change, and the phase changes by π/2. It can be shown that in this case

$$\eta_{-}(t) = \frac{1}{\pi} \int_{-\infty}^{\infty} \frac{\eta_{+}(t')}{t' - t + \sqrt{\frac{4L}{g\alpha}}} dt' \quad . \tag{8}$$

The last term in the denominator can be eliminated by redefining the zero of the time. This solution was first obtained by using Hilbert transformations in works [Mazova, 1984; Volzinger et al., 1989].
Thus, for a plane slope, for an arbitrary initial perturbation, the solution for the reflected wave will have the form

$$\eta_{ref}(t) = \frac{1}{\pi} \int_{-\infty}^{\infty} \frac{\eta_{inc}(t')}{t' - \tau} dt' \quad . \tag{9}$$

3. CALCULATION OF THE ANALYTICAL MODEL OF THE REFLECTED WAVE.

For example, consider the reflection of a single wave from a plane slope (the Lorentz momentum) [Mazova, 1984], whose spectrum has the following form

$$H(\omega) = \frac{1}{4} e^{-\frac{|\omega|}{2} + i\theta} \quad . \tag{10}$$

The reflected wave is obtained by means of the Hilbert transform, where the initial perturbation is calculated by formula

$$\eta_{inc} = \int_{-\infty}^{\infty} H(\omega) e^{i\left(\omega t - \frac{\pi}{4}\right)} d\omega \quad , \tag{11}$$

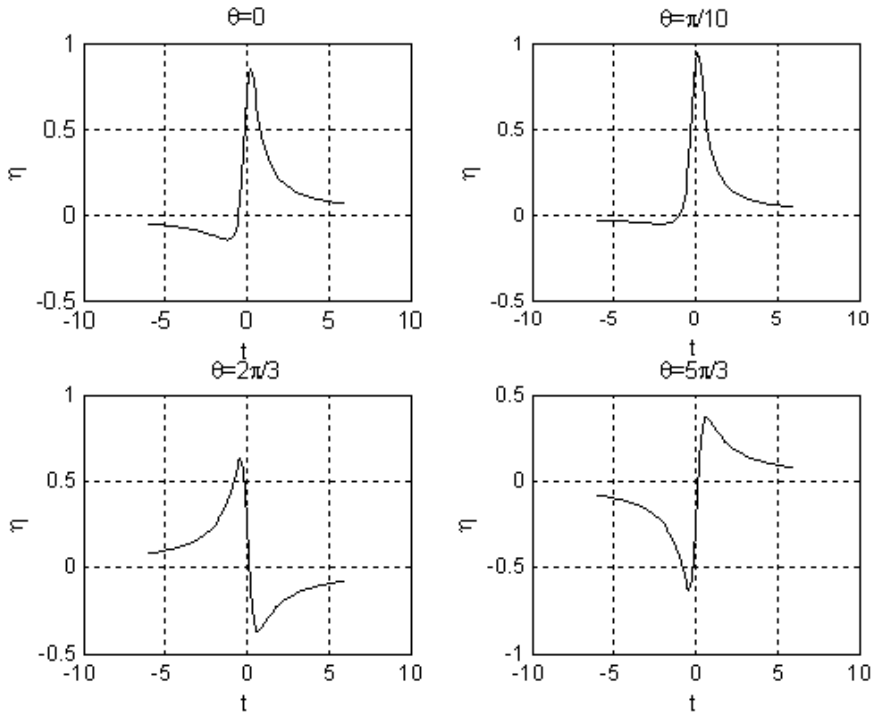

Fig. 2. Tide-gauge records of incident wave for θ: 0; π/10; 2π/3; 5π/3.

Figures 2 and 3 show tide-gauge records for the incident and reflected waves for various values of the parameter θ (see formulas (11) and (9)). As can be seen from the figures, the shape of the reflected wave changes significantly in comparison with the shape of the incident wave when θ changes [Mazova, 1984].

4. REFLECTED WAVES FROM THE SLOPE - CONJUGATED WITH PLANE BOTTOM

Reflection for a monochromatic wave. In the region of a constant depth $x > x_1$ (Fig. 4), the solution of equation (2) for a monochromatic wave is represented as a superposition of the incident and reflected waves [Mazova, 1984]

$$\eta_1(x,t) = Ae^{i(\omega t - kx_1)} + Be^{i(\omega t + kx_1)}, \tag{12}$$

where $k = \frac{2\pi}{\lambda}$, $\omega = k\sqrt{gh}$ (h = const), A and B are amplitudes of incident and reflected waves, respectively. Here, second term corresponds to the solution for reflected wave.

$$\eta_{ref} = Be^{i(\omega t + kx_1)}. \tag{13}$$

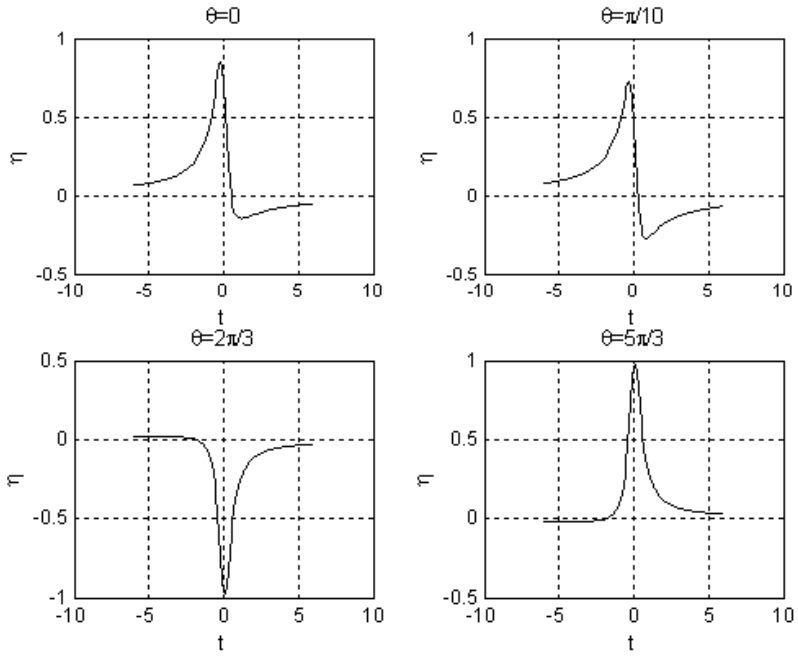

Fig. 3. Tide-gauge records of reflected wave for θ: 0; π/10; 2π/3; 5π/3

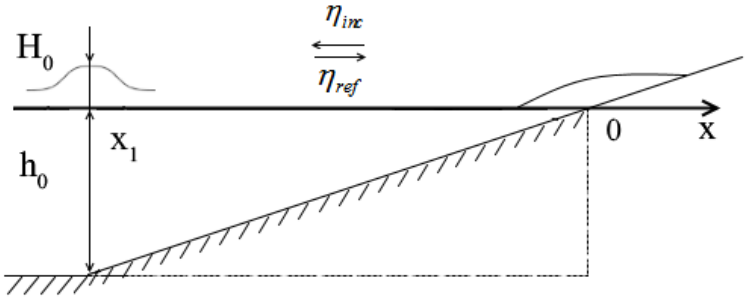

Fig.4. The geometry of the problem for a sloping beach - conjugated with even bottom.

The solution for plane slope $0 < x < x_1$ can be wrote via the Bessel function

$$\eta_2(x,t) = \left[\ C \cdot J_0(z) + D \cdot N_0(z)\ \right] e^{i\omega t}, \tag{14}$$

where $z = \sqrt{\frac{4\omega^2 |x|}{g\alpha}}$, α is the inclination angle of the plane slope, J_0 is the first kind Bessel function, N_0 is the Neumann function, and C and D are arbitrary constants. Because the solution must be

bounded everywhere, including at the shoreline ($x = 0$), then it is necessary to require $D = 0$, since the function N_0 has a logarithmic singularity for $x = 0$. Then

$$\eta_2(x,t) = C \cdot J_0(z) \cdot e^{i\omega t}. \tag{15}$$

The boundary conditions in the point $x = x_1$ can be obtained using system of linear shallow water equations

$$\begin{cases} \dfrac{\partial \eta}{\partial t} + \dfrac{\partial}{\partial x}(hu) = 0, \\ \dfrac{\partial u}{\partial t} + g\dfrac{\partial \eta}{\partial x} = 0 \end{cases} \tag{16}$$

by integrating (16) we will obtain

$$\begin{aligned} &\frac{\partial}{\partial t}\int \eta\, dx + hu\Big|_{-}^{+} \Rightarrow h_1 u_1^{left} = h_1 u_1^{right} \\ &\frac{\partial}{\partial t}\int u dx + g\eta\Big|_{-}^{+} \Rightarrow \eta_1^{left} = \eta_1^{right}, \end{aligned} \tag{17}$$

where $\dfrac{\partial}{\partial t}\int \eta\, dx \to 0$ or $\dfrac{\partial}{\partial t}\int u dx \to 0$.

Using the continuity conditions at the point x_1 for the displacement of the water points and the equality of the water mass flows, we "sew" these solutions at the point $x = x_1$ (or $x = L$, where L is the shelf length)

$$\begin{cases} \eta^{left} = \eta^{right}, \\ h_1 u_1^{left} = h_1 u_1^{right}. \end{cases} \tag{18}$$

In the point $x = x_1$, using condition of equality of water point displacement $\eta^{left} = \eta^{right}$

$$Ae^{-i(\omega t - kx)} + Be^{-i(\omega t + kx)} = J_0(z_1)Ce^{i\omega t}, \tag{19}$$

where $k = \dfrac{\omega}{\sqrt{gh}}$

$$Ae^{-ikx_1} + Be^{ikx_1} = CJ_0(z_1),$$

rewrote in the form

$$Be^{ikx_1} - CJ_0(z_1) = -Ae^{-ikx_1}. \tag{20}$$

In the point $x = x_1$, using condition of equality of water mass $h_1 u_1^{left} = h_1 u_1^{right}$ and from (16) at $u(x,t) = u(x)e^{i\omega t}$, we will obtain

$$i \cdot \omega \cdot u = -g \frac{\partial \eta}{\partial x} \Rightarrow u = -\frac{g}{i\omega} \frac{\partial \eta}{\partial x},$$

then

$$u_1^{left} = -\frac{g}{i\omega} \frac{\partial \eta_1^{left}}{\partial x} = -\frac{g}{i\omega} \left[-ikAe^{i(\omega t - kx_1)} + ikBe^{i(\omega t + kx_1)} \right],$$

$$u_1^{right} = -\frac{g}{i\omega} \frac{\partial \eta_1^{right}}{\partial x} = -\frac{g}{i\omega} \cdot C \frac{\partial J_0}{\partial z} \frac{dz}{dx}.$$

Since

$$\frac{\partial J_0}{\partial z} = -J_1(z_1),$$

we will obtain

$$\frac{dz}{dx} = -\frac{1}{2} x^{-1/2} \sqrt{\frac{4\omega^2}{g\alpha}} = \frac{\omega}{\sqrt{g\alpha x_1}},$$

and from (16)

$$u_1^{right} = -\frac{g}{i\omega} C \cdot J_1(z_1) \frac{\omega}{\sqrt{g\alpha x_1}} = \frac{g}{i\omega} C \cdot J_1(z_1) \cdot k.$$

Since

$$h_1^{left} = h_1^{right},$$

then

$$u_1^{left} = u_2^{right}.$$

By equating,

$$-\frac{g}{i\omega} \left[-ikAe^{i(\omega t - kx_1)} + ikBe^{i(\omega t + kx_1)} \right] = -\frac{g}{i\omega} \cdot C \cdot J_1(z_1) \cdot k$$

we have

$$-iAe^{-ikx_1} + iBe^{ikx_1} = C \cdot J_1(z_1), \quad iBe^{ikx_1} - C \cdot J_1(z_1) = iAe^{-ikx_1}$$

or

$$Be^{ikx_1} + i \cdot C \cdot J_1(z_1) = Ae^{-ikx_1}. \qquad (21)$$

By writing solutions (20) or (21)

$$\begin{cases} Be^{ikx_1} - C \cdot J_0(z_1) = -Ae^{-ikx_1}, \\ Be^{ikx_1} + i \cdot C \cdot J_1(z_1) = Ae^{-ikx_1}, \end{cases}$$

we can find coefficient C

$$C = \frac{\begin{vmatrix} e^{ikx_1} & -Ae^{-ikx_1} \\ e^{ikx_1} & Ae^{-ikx_1} \end{vmatrix}}{\begin{vmatrix} e^{ikx_1} & -J_0(z_1) \\ e^{ikx_1} & iJ_1(z_1) \end{vmatrix}} = \frac{2A}{iJ_1(z_1)e^{ikx_1} + J_0(z_1)e^{ikx_1}} = \frac{2A}{J_0(z_1) + iJ_1(z_1)} \cdot \frac{1}{e^{ikx_1}} =$$

$$= \frac{2A}{\sqrt{J_0^2(z_1) + iJ_1^2(z_1)}} \cdot \frac{1}{e^{iarctg(-J_1/J_0)}} \cdot \frac{1}{e^{ikx_1}} = \frac{2A}{\sqrt{J_0^2(z_1) + iJ_1^2(z_1)}} e^{-i\left[kx_1 - arctg\left(\frac{J_1(z_1)}{J_0(z_1)}\right)\right]} =$$

$$= \frac{2A}{\sqrt{J_0^2 + iJ_1^2}} e^{-i\left[kx_1 - arctg\left(\frac{J_1}{J_0}\right)\right]}.$$

By designating for $H_0 = \frac{2A}{\sqrt{J_0^2 + iJ_1^2}}$, we will obtain solution for reflected wave

$$\eta_{ref} = H_0 e^{-2i\left[kx_1 - arctg\frac{J_1}{J_0}\right]} e^{i\omega t} = H_0 e^{-i\left[(2kx_1 - \omega t) - 2arctg\frac{J_1}{J_0}\right]}. \quad (22)$$

Reflection of the pulse of arbitrary form. Using the Fourier transformation

$$\int_{-\infty}^{\infty} \eta_{ref}(t') e^{-i\omega t'} dt' = 2\pi \cdot H(\omega) \quad , \tag{23}$$

we will obtain

$$\eta_{ref}(t) = \int_{-\infty}^{\infty} H(\omega) \cdot e^{-i\left[\left(2kx_1 - \omega t\right) - 2arctg\frac{J_1}{J_0}\operatorname{sgn}\omega\right]} d\omega \quad . \tag{24}$$

By substituting (23) to (24), we will have

$$\eta_{ref}(t) = \frac{1}{2\pi} \int_{-\infty}^{\infty} \eta_{inc}(t') e^{i\omega(t-t')} dt' \int_{-\infty}^{\infty} e^{2i\omega(t-t')} e^{2iarctg\frac{J_1}{J_0}\operatorname{sgn}\omega} d\omega \tag{25}$$

or

$$\eta_{ref}(t) = \frac{1}{2\pi} \int_{-\infty}^{\infty} \eta_{inc}(t') dt' \int_{-\infty}^{\infty} e^{i\left[2arctg\frac{J_1}{J_0}\operatorname{sgn}\omega - \omega(t-t')\right]} d\omega \quad . \tag{26}$$

By taking inner integral for Green function

$$G(t-t') = \int_{-\infty}^{\infty} e^{i\left[2arctg\frac{J_1}{J_0}\operatorname{sgn}\omega - \omega(t-t')\right]} d\omega \quad , \tag{27}$$

We will solve in the form

$$\eta_{ref} = \frac{1}{2\pi} \int_{-\infty}^{\infty} \eta_{inc}(t') dt' \cdot G(t-t') \quad . \tag{28}$$

Rewriting Green function in the following form

$$G(t-t') = \int_{-\infty}^{\infty} K_{ref}(\omega) e^{i\omega\left(t-t'\right)} d\omega \quad , \tag{29}$$

where $K_{ref}(\omega) = e^{-i2arctg\frac{J_1}{J_0}}$ is the reflection coefficient.

Using asymptotic expansions of Bessel functions at infinity and for small values of the argument

$$J_0(z)=\begin{cases}1-\dfrac{z^2}{4}, & z\to 0,\\ \sqrt{\dfrac{2}{\pi\cdot z}}\cos(z-\dfrac{\pi}{4}), & z\to\infty,\end{cases}\qquad J_1(z)=\begin{cases}\dfrac{z}{2}, & z\to 0,\\ \sqrt{\dfrac{2}{\pi\cdot z}}\sin(z-\dfrac{\pi}{4}), & z\to\infty,\end{cases} \tag{30}$$

after a simple transformation

$$\frac{J_1}{J_0}\approx\begin{cases}\dfrac{z}{2}, & z\to 0,\\ tg(z-\dfrac{\pi}{4}), & z\to\infty,\end{cases} \tag{31a}$$

$$arctg\frac{J_1}{J_0}\approx\begin{cases}arctg\dfrac{z}{2}\approx\dfrac{z}{2}, & z\to 0,\\ z-\dfrac{\pi}{4}, & z\to\infty,\end{cases} \tag{31b}$$

it is possible to evaluate the obtained solution (26) for two limiting cases: $z\to 0$ - reflection of a wave from a vertical wall and $z\to\infty$ - reflection from a plate slope. The first solution is well known for linear formulation of the problem, and the second is obtained above. So, for $z\to 0$ ($x\to\infty$) from (27) we have

$$G(t-t')=\int_{-\infty}^{\infty} e^{i2arctg\frac{J_1}{J_0}} e^{i\omega\left(t-t'\right)}d\omega . \tag{32}$$

Further, with taking into account (30), first multiplier under in integral becomes to be equal unity, and remaining integral is well known

$$\int_{-\infty}^{\infty} e^{i\omega\left(t-t'\right)}d\omega=2\pi\cdot\delta(t-t') . \tag{33}$$

Hence, from (26) we obtain that at $z\to 0$ the Green function is transformed to the δ-function

$$G(t-t')=2\pi\cdot\delta(t-t') \tag{34}$$

and, substituting this expression to (25), we finally have

$$\eta_{ref}(t) = \frac{1}{2\pi}\int_{-\infty}^{\infty}\eta_{inc}(t')dt' \cdot 2\pi \cdot \delta(t-t') = \int_{-\infty}^{\infty}\eta_{inc}(t')\delta(t-t')dt' = \eta_{inc}(t') \quad . \tag{35}$$

Thus, at $z \to 0$ we obtain a classical solution to the problem of a long wave runup to a vertical wall in a linear formulation [Zheleznyak, 1985]

$$\eta_{ref} = \eta_{inc} \quad . \tag{36}$$

For the case of the plane slope ($z \to \infty$), using (30), we will consider

$$G(t-t') = 2\int_{-\infty}^{\infty} e^{2iarctg\frac{J_1}{J_0}} e^{i\omega(t-t')}d\omega = -i\int_{-\infty}^{\infty} e^{i\omega(t-t')}d\omega = 2(-i)\frac{1}{t-t'}\frac{(-1)}{(-i)} = \frac{2}{(t-t')} \quad . \tag{37}$$

Substituting (37) to (26), we obtain [Pelinovsky, 1982; Mazova, 1984]

$$\eta_{ref}(t) = \frac{1}{\pi}\int_{-\infty}^{\infty}\frac{\eta_{inc}(t')}{t-t'}dt' \quad . \tag{38}$$

Thus, from general solution (22) the solution for two limited cases was obtained: $z \to 0$ and $z \to \infty$.
Let us now consider the case of small deviations from a vertical wall and compare it with particular solutions for such a case (see [Mazova, 1984, Voltsinger et al., 1989]). Rewrite the reflection coefficient (see (28)

$$K_{ref}(\omega) = e^{-i2arctg\frac{J_1}{J_0}} \quad . \tag{39}$$

Taking into account the expansion of exponent in small parameter series, we will have

$$K_{ref}(\omega) = 1 - i\cdot 2arctg\frac{J_1}{J_0} - \frac{4}{2!}arctg^2\frac{J_1}{J_0} + \ldots \quad , \tag{40}$$

then, taking into account the expansion (31a) and (31b), and restricting by members of the second order, we will obtain:

$$\mathrm{Re}\,K_{ref}(\omega) = \begin{cases} 1 - z^2, & z \to 0, \\ 1 - 2(z - \frac{\pi}{4})^2 & z \to \infty. \end{cases} \tag{41}$$

Designating for $\gamma = 2\sqrt{\frac{|x|}{g\alpha}}$, we have $z = 2\omega\sqrt{\frac{|x|}{g\alpha}} = \gamma\omega$.

Then, (41) will be rewritten as

$$\mathrm{Re}\, K_{ref}(\omega) = \begin{cases} 1-\gamma^2\omega^2, & z \to 0, \\ 1-2(\gamma\omega - \frac{\pi}{4})^2, & z \to \infty. \end{cases} \tag{42}$$

Returning to the Green function (27) and taking into account we will have

$$G(t-t') = \int_{-\infty}^{\infty} e^{-i\omega(t-t')}(1-\gamma^2\omega^2)d\omega \tag{43}$$

or

$$G(t-t') = \int_{-\infty}^{\infty} e^{-i\omega(t-t')}d\omega - \gamma^2 \int_{-\infty}^{\infty} \omega^2 e^{-i\omega(t-t')}d\omega \,. \tag{44}$$

Since first term in this expression is

$$I_1 = \int_{-\infty}^{\infty} e^{-i\omega(t-t')}d\omega = 2\pi\cdot\delta(t-t') \,, \tag{45}$$

and second one can be easy transformed by following manner

$$I_2 = \int_{-\infty}^{\infty} \omega^2 e^{-i\omega(t-t')}d\omega = -\int_{-\infty}^{\infty} \frac{\partial^2}{\partial t^2} e^{-i\omega(t-t')}d\omega =$$

$$= -\frac{\partial^2}{\partial t^2}\int_{-\infty}^{\infty} e^{-i\omega(t-t')}d\omega = -\frac{\partial^2}{\partial t^2} 2\pi\cdot\delta(t-t'), \tag{46}$$

then (44) can be rewrote in the following form

$$G(t-t') = \left(1-\gamma^2\frac{\partial^2}{\partial t^2}\right)\cdot 2\pi\cdot\delta(t-t') \,.$$

From here, we have:

$$\eta_{ref} = \frac{1}{2\pi}\int_{-\infty}^{\infty}\eta_{inc}(t')\left(1+\gamma^2\frac{\partial^2}{\partial t^2}\right)\cdot 2\pi\cdot\delta(t-t')dt' =$$

$$= \frac{1}{2\pi}\cdot 2\pi\left(1+\gamma^2\frac{\partial^2}{\partial t^2}\right)\int_{-\infty}^{\infty}\eta_{inc}(t')\delta(t-t')dt' = \left(1+\gamma^2\frac{\partial^2}{\partial t^2}\right)\cdot\eta_{inc}(t). \quad (47)$$

Finally, we have

$$\eta_{ref}(t) = \eta_{inc}(t) + \gamma^2\frac{d^2\eta_{inc}}{dt^2} = (1+\gamma^2\frac{d^2}{dt^2})\eta_{inc}, \qquad \gamma = 2\sqrt{\frac{|x|}{g\alpha}}. \quad (48)$$

This solution agrees well with the analogous result from the work on wave reflection in the boundary layer theory [Sugimoto, Kakutani, 1984, 1988] for the case of steep slopes, where the coefficient in front of the second-order term in the differentiation operator is equal to $\mu^2/2$, and $\mu = h/\mathrm{ctg}\alpha$ is a dimensionless quantity. The quantity γ in (48) has the dimension of time. The relation between μ and γ is easy to find: $\gamma = 2\mu\tau^*$, where the introduced quantity $\tau^* = l/\sqrt{gh}$ has the meaning of a characteristic time, and l of a characteristic length.

Thus, the solution (48) is a solution for the reflected wave from the slope, which is conjugated with even bottom for any slope angles. The solution is valid for any form of the initial perturbation in the source to obtain extreme rundown characteristics.

Below are the figures (Fig. 5, Fig. 6) of the incident and reflected waves, calculated from the formula (26) for different values of the parameter θ.

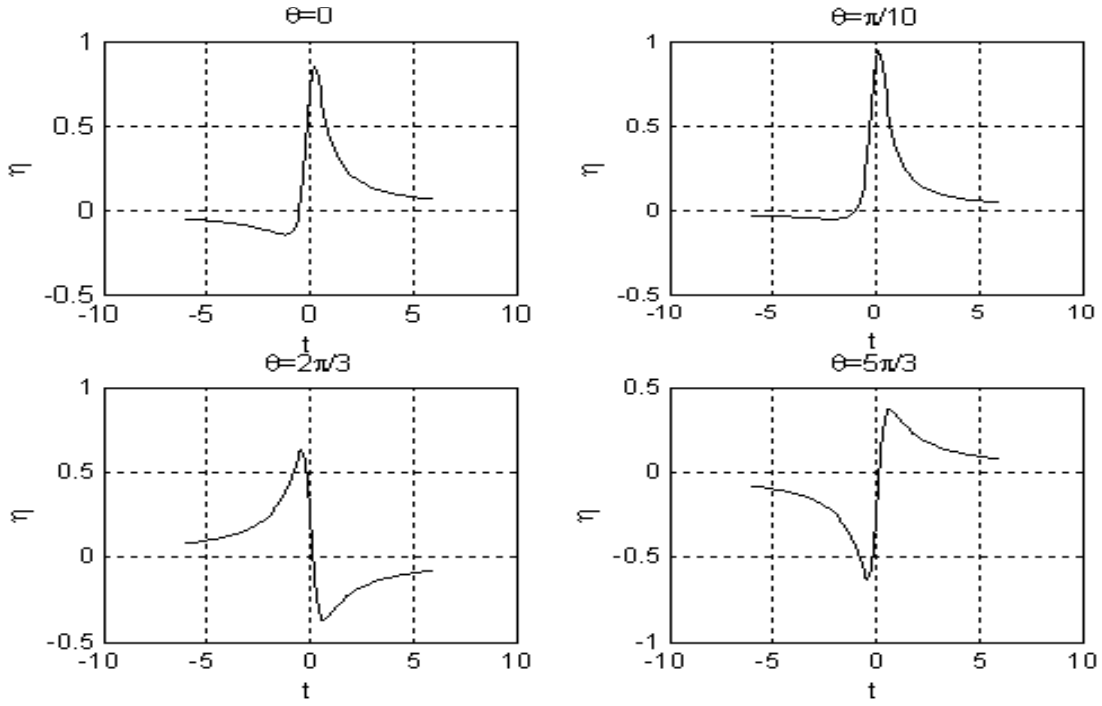

Fig. 5. Tide-gauge records of incident wave for θ: 0; π/10; 2π/3; 5π/3.

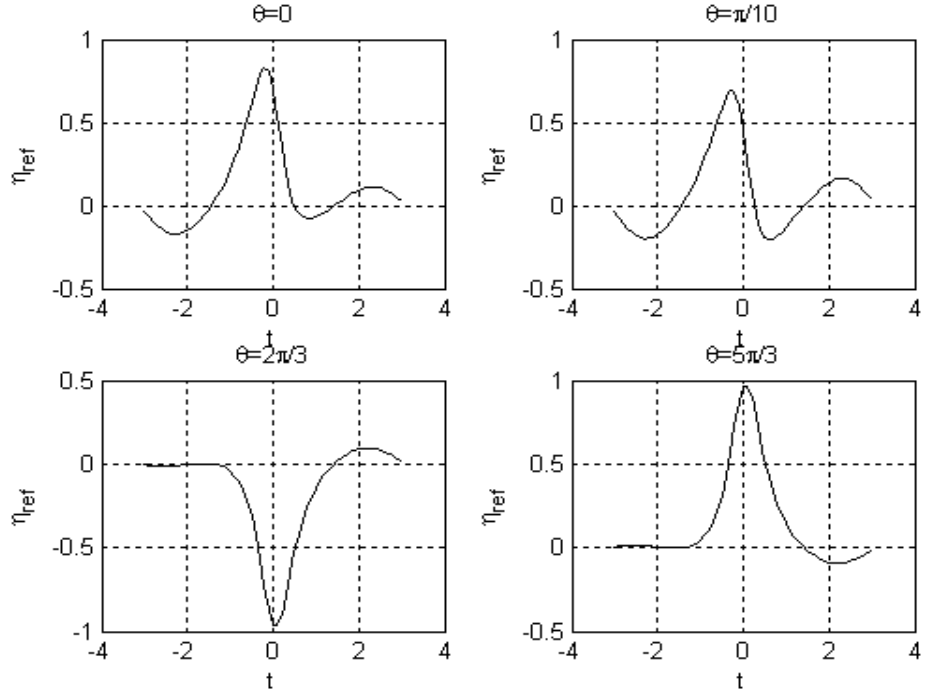

Fig. 6. Tide-gauge records of reflected wave for θ: 0; π/10; 2π/3; 5π/3.

In Fig.7 it is presented an incident wave given by expression (11) and computation on analytical formula (28).

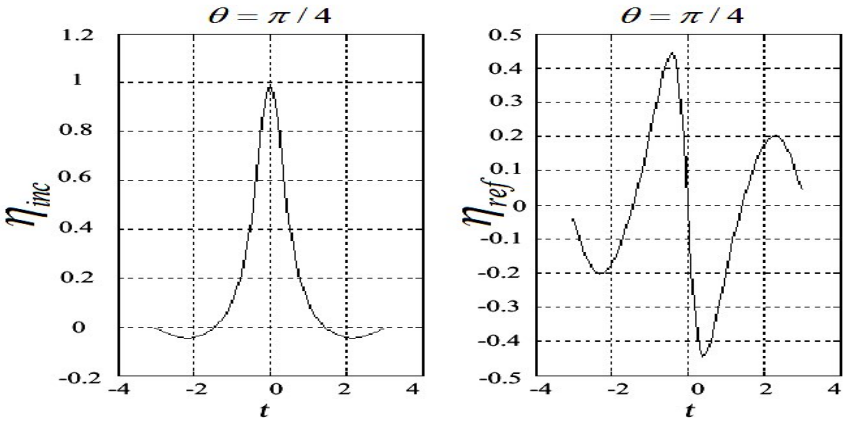

Fig. 7. The incident wave given by expression (11) and calculation by the analytical formula (47) for θ = π / 4.

5. CALCULATION OF THE REFLECTION COEFFICIENT

For the Lorentz pulse, the reflection coefficient determined by the ratio of the incident and reflected waves was also calculated (see, for example, [Synolakis, 1987])

$$\eta_{ref} = \eta_{inc} \cdot K(\omega), \tag{49}$$

and also by formula (38) obtained in the analytic solution of our problem. As seen from Fig. 8, both dependences are in good agreement, including in the initial part of the curves, where the dependence is quadratic in character.

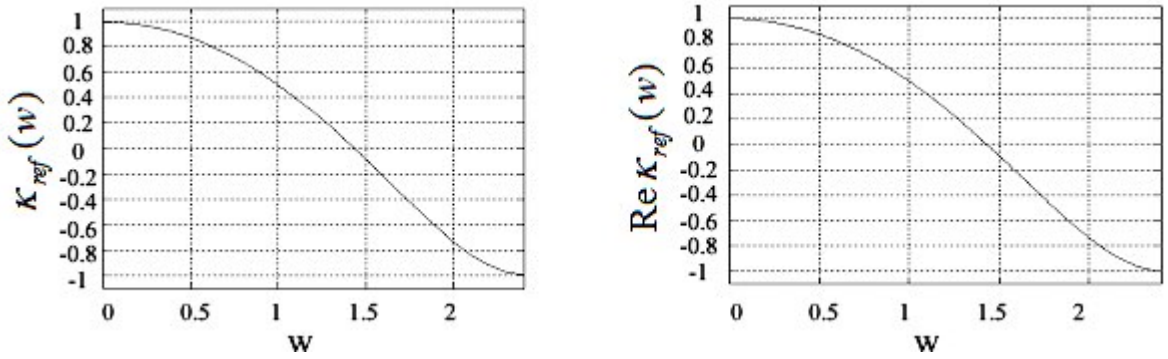

a) *b)*

Fig. 8. The reflection coefficient for complex slope for *θ*: a) 0; π/10; 2π/3; 5π/3 according to the formulas (39); b) by formula (49).

6. NUMERICAL SIMULATION OF THE REFLECTED WAVE FROM THE SLOPE, CONJUGATED WITH EVEN BOTTOM

Figure 9 shows an example of the results of numerical modeling of the runup process and the formation of a reflected wave for the Lorentz pulse (see above) of a specific shape and typical parameters of the coastal slope. The calculation was carried out in an oblique coordinate system (scheme 35 [Marchuk et al., 1983]). As can be seen from the figure, in this case the observed value of the crest in the dipolar wave forming in the process of rundown ($t \approx 45, 46$) of the order of its amplitude in a coming wave in the runup phase ($t = 40$). At the same time, behind the crest, leaving in the direction of deep water, there is a well-observed depression. It is also clearly seen that at smaller times ($t \approx 43, 44$), as already mentioned above, the incident and reflected waves can not be differentiated from each other. At long calculation times, although the waveform approaches the initial wave, but with smaller amplitude, and oscillations at the trailing edge of the cavity formed during the reflection process. The observed picture is in good agreement with the available results of both the analytical study of the process and the numerical modeling of the runup of a single pulse with taking into account of reflection (see, for example, [Zheleznyak, 1985, Synolakis, 1987]).

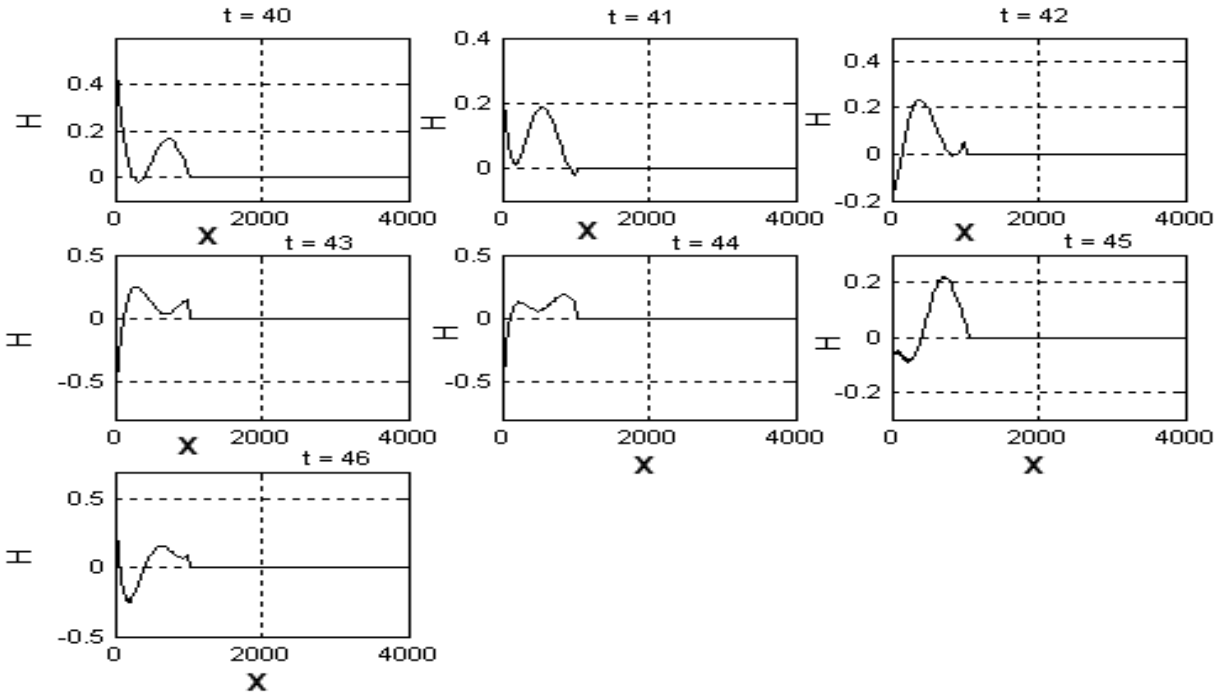

Fig. 9. Numerical simulation of the reflection process of the Lorentz pulse from the slope.

7. CONCLUSION

The analysis of the characteristics of the long gravitational wave (tsunami) reflected from the sloping beach in the framework of the theory of shallow water allows us to indicate the main features of the process of runup in the coastal region. The results obtained were tested for the case of a Lorentzian pulse (with different phases of the wave), and a good agreement was obtained with the data available in the literature. In the case of a slope, conjugated with a even bottom, limiting cases of low and high frequencies are analytically investigated, and numerical calculations of the behavior of the reflection coefficient on the whole frequency interval are also carried out. Analytical and numerical results are consistent; the reflection coefficient of low frequencies is a quadratic function of frequency.

Such a result agrees with the conclusions of similar studies of the reflection process in the framework of the "edge layer" theory. A comparison is made with numerical calculations of the reflection of a soliton from a vertical wall, and a qualitative agreement is obtained. Numerical modeling of the reflection process from a sloping beach conjugated with even bottom is carried out according to available programs. Good agreement with analytical results and available results of laboratory modeling is obtained.

ACKNOWLEDGEMENTS

This work was supported by the grant of the President of the Russian Federation No. NSh-2685.2018.5.

REFERENCES

1. Belokon V.I., Semkin S.V., On the coefficient of reflection of tsunami waves for some forms of the bottom relief // Tsunami Investigation, Moscow, 1998, No.5, p. 66-70.
2. Voltsinger N.E., Klevannyi K.A., Pelinovsky E.N. Long-wave dynamics of the coastal zone, Leningrad, USSR.: Gidrometeoizdat, 1989.- 272 p.
3. Kozlov S.I. On the runup of a tsunami wave to a coast without breaking, Izv. AN SSSR. FAO v.17, p.996, 1981.
4. Mazova R.Kh. On approximate boundary conditions on the shoreline that are convenient for numerical simulation of the tsunami wave runup // in: Generation of tsunami waves and wave output to shore, Moscow, USSR: Radio and Communications, 1984, pp. 54-57. (1984)
5. Pelinovsky, E. N., Nonlinear dynamics of tsunami waves, Gorky: ed. IAP of the USSR Academy of Sciences, 1982. - 226 p.
6. Sugimoto N., Kakutani T. Reflection of a shallow-water solution. Part 1. Edge layer for shallow-water waves // J. Fluid Mech. V.146, P.369-375, 1984.

7. Sugimoto., Kakutani T. Reflection of a shallow-water solution. Part 1Edge layer for shallow-water waves // J. Fluid Mech. V.146, P.369-375, 1984.
8. C.E.Synolakis The run-up and reflection of solitary waves \\ In Proc, ASCE Conf. on Coastal Hydrodyn, Univ. of Delaware, \\ Newark, 1987, pp.533-547.
9. A.Jeffrey., H.H.Dai, On the reflection of a solitary wave at a sloping beach: analytical results, Wave Motion V.10, P.375, 1988.
10. Dai H.H., A.Jeffrey, Reflection of interface solitary waves at a slope // Wave Motion V.11, P.463, 1989.
11. Zheleznyak M.I., The effect of long waves on continuous vertical obstacles, in the book: Nakat tsunami on the shore, Gorky, IAP Academy of Sciences of the USSR, 1985, p. 122.
12. Mazova R.Kh., Pelinovsky E.N. Linear theory of the wave of tsunami waves on the shore, Izvestiya of USSR Academy of Sciences, Atmosphere and Ocean Physics, 18, 166, 1982.
13. Mazova R.Kh., Pelinovsky E.N., Shavratsky S.N. One-dimensional theory of the wave runup of tsunami waves on the shore, in: Processes of generation and propagation of tsunami waves. Moscow, USSR, 1982, p.98.
14. Mazova R.H. Reflection of tsunami waves from the slope // Tsunami Meeting, Gorky, IAP of the USSR Academy of Sciences, 1984, Abstr.Book, pp. 103-105. (1984)
15. Gradshtein IS, Ryzhik IM Tables of integrals, sums, series and products, Moscow, USSR: GIFML, 1963. - 1100 p.
16. Marchuk A.G., Chubarov L.B., Shokin Yu.I. Numerical modeling of tsunami waves (Nauka Press, Novosibirsk, USSR, 1983).

ISSN 8755-6839

SCIENCE OF **TSUNAMI HAZARDS**

Journal of Tsunami Society International

Volume 37 **Number 4** **2018**

ANALYSIS OF TRAVEL TIME DELAY FOR LARGE TSUNAMIS ACROSS THE PACIFIC AND INDIAN OCEANS

Tjipto Prastowo[1,2], Latifatul Cholifah[2], Madlazim[1,2]

[1]Physics Department, State University of Surabaya, Surabaya 60231, Indonesia
[2]Center for Earth Science Studies, State University of Surabaya, Surabaya 60231, Indonesia
Correspondence: madlazim@unesa.ac.id

ABSTRACT

Travel time delay for a tsunami has been an increasingly important issue in recent years. The delay in time is calculated from a difference in arrival times between simulated waveforms and waves recorded by DART and gauge stations. In this study, we estimate travel times for the 2011 Tohoku, the 2014 Iquique, the 2004 Aceh, and the 2010 Mentawai events. We compare estimated travel times with travel times from field records and find that the time delay is increasing with epicentral distance, following reduced speeds during propagation. From analyses of the delays, we conclude that speed reduction in the Pacific is 1-2% from the long-wave speed but twice larger or more in the Indian Ocean due to its complex bathymetry. For far-field propagation in the Pacific, the delays could be approximately 17 minutes whereas the same amount of delay was attained at a shorter distance in the Indian Ocean.

Keywords: *travel time delay, estimated travel times, epicentral distance, speed reduction*

Vol 37. No. 4, page 195 (2018)

1. INTRODUCTION

Disaster early warning issues are of primary importance in the sense that the accurate and quick release of early warning may prevent society from potential losses of lives, properties, and infrastructures. The occurrence of a tsunami wave on a beach, for example, needs to be predicted accurately using rapid assessment of tsunami waveforms recorded by in-situ instruments and theoretical development of tsunami propagation modeling. In this regard, this current work examines arrival times of a tsunami wave detected by a regional network of seismic stations either positioned nearby or at far away from the source location. With respect to tsunami onset times, these quantities lead to observed travel times of tsunami wave propagation at an open sea. In the context of hazard mitigation study, particularly critical problems with disaster preparedness and risk reduction efforts for vulnerable countries in the Indian Ocean zone (Suppasri et al. 2015), knowledge of accurate travel times, both measured and predicted, is required for minimizing possible fatalities imposed by such a catastrophy (Cholifah and Prastowo, 2017).

Regarding the above backgrounds, research focusing upon the difference in travel times between observed waves and simulated waveforms has thus been an increasingly important issue in recent years. Since then, many researchers (e.g., Wessel, 2009; Inazu and Saito, 2013; Allgeyer and Cummins, 2014; Wang, 2015) have reported that trans-oceanic large tsunamis propagating across the ocean with a total travel distance of exceeding thousands kilometers away show a departure of observed travel times from predicted values based on the shallow-water, long-wave theory. This departure is called travel time delay in the present study, which is arguably attributed to variations in tsunami phase speed, as addressed in previous studies (Tsai et al. 2013; Watada, 2013; Watada et al. 2014; Gusman et al. 2015). All of these studies have used a combined method of exploring tsunami numerical modeling with some assumptions to take into account for the linear approximation and field data observations for comparison.

In the following sections, we provide basic physics principles for shallow-water, long-wave approximation usually made for use of numerical modeling of tsunami wave propagation at an open sea (Fine et al. 2013; Heidarzadeh et al. 2014). Seawater is assumed to be incompressible and homogeneous with no vertical stratification (see, for example, Wang, 2015) and hence vertical profile of seawater density is assumed to be constant with depth. There is no shear at both the sea surface and sea bottom, and hence effects of wind-induced forcing and other external influences are not included in the governing equations. In the absence of local circulation in the ocean by diffusion (Prastowo et al. 2017), the only driving force for the horizontal advection of massive mass and volume fluxes of seawater is seismic energy released from fault movement at depth. Vertical variation in the sea surface elevation is merely considered to be important during the passage of a gigantic tsunami wave that propagates over a long distance along a stationary, flat-bottomed seafloor. However, tsunami wave height or its corresponding wave amplitude is assumed to be relatively small compared with

tsunami wavelength and water depth (Cholifah and Prastowo, 2017). Therefore, the small-amplitude wave theory during tsunami propagation remains useful. Non-linearity effects of higher-order terms imposed by the free sea surface and rigid bottom boundary conditions in the equations of motion are also negligible.

All of the above assumptions lead to the well-known linear, shallow-water, long-wave propagation of a tsunami wave, written as momentum equation below

$$\partial \mathbf{u}/\partial t = - g d\, (\partial/\partial x + \partial/\partial y)\eta \qquad (1)$$

where $\mathbf{u}$ is the depth-integrated horizontal velocity of the wave with $\partial \mathbf{u}/\partial t$ represents the tsunami speed evolution with time, g is gravitational acceleration due to the Earth's gravity, d is the ocean depth, and η is the sea surface elevation. The corresponding continuity equation is as follows,

$$\partial \eta/\partial t + (\partial/\partial x + \partial/\partial y)\mathbf{u} = 0 \qquad (2)$$

simply describing conservation of mass for incompressible fluid of seawater (see Prastowo and Ain, 2015). After some simple algebra, the theoretical speed c of a propagating tsunami can be obtained as follows,

$$c = (g d)^{1/2} \qquad (3)$$

For a typical water depth of $d \sim 5$ km, the tsunami speed is about 720 km/h.

Inazu and Saito (2013) proposed a local parameter β taken into account from loading effects of seafloor deformation. This parameter introduces the roles of non-stationary sea bottom over bathymetry in the form of a reduced wave height $\eta - \eta_o$ measured from the sea surface into the momentum equation, where η_o is associated with the depth through which seabed is deformed. Equation (1) then becomes

$$\partial \mathbf{u}/\partial t = - g d\, (\partial/\partial x + \partial/\partial y)(\eta - \eta_o) \qquad (4)$$

with equation (2) remains true but with an additional equation relating η to η_o via the β parameter, that is, $\eta = \beta \eta_o$ over which tsunami speed reduction due to the Earth elasticity is in effect. Wang (2015) further explained that β was found to be relatively small to account for the depth-corrected speed of only 1% from the theoretical long-wave speed. This parameter limits the observed speed to

only a small amount of tsunami speed reduction for near-field and far-field (Inazu and Saito, 2013; Wang, 2015) according to

$$c = (gd)^{1/2}\ (1-\beta)^{1/2} \tag{5}$$

Noting that equation (5) is particularly applicable to distant observations, we here argue that the speed is reduced while propagating over large distances across the ocean with complex bathymetry, as suggested by Tsai et al. (2013) and Watada (2013). This speed reduction is observed as the apparent difference in tsunami travel time between numerical simulations (*e.g.*, Allgeyer and Cummins, 2014; Watada et al. 2014; Gusman et al. 2015) and field observations by monitoring Deep-ocean Assessment Reports of Tsunamis (DART) buoys and tide-gauge instruments.

In this study, we extract estimates of tsunami travel times from tsunami waveforms of four large tsunami events that occurred in the Pacific and Indian Oceans and then compare estimated travel times with observed travel times from field records obtained from wide-spread network of coastal and mainland observatories using either DARTs or tide gauges. We carefully examine and analysis the delay in time derived for each case considered in relation to increasing travel distance. Therefore, the primary aims of the present study are to see if there is a systematic increase in the delays with epicentral distance for all trans-oceanic tsunamis examined in this study and to determine whether the increase is associated with speed reduction, as predicted by equation (5).

2. METHOD

The methods used in this study included procedures for research design, as shown in Figure 1, numerical data collection from observed waves and simulated waveforms, and data analysis technique.

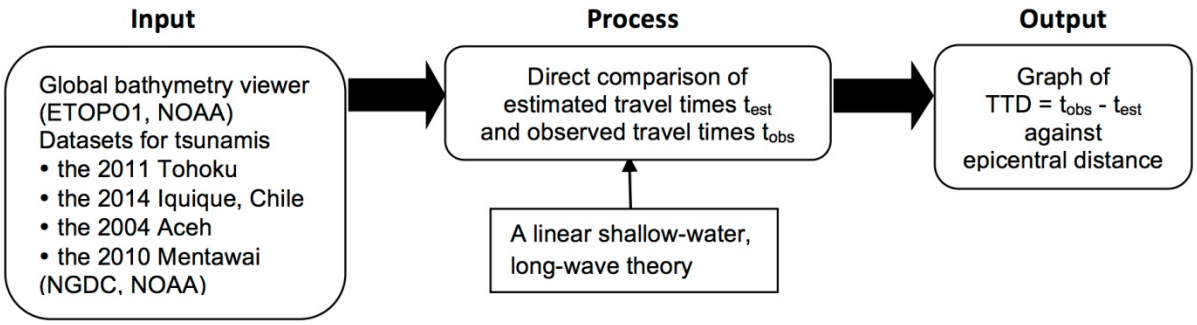

Figure 1. Simple diagram, showing steps at obtaining travel time delay (TTD) against epicentral distance.

We examined four cases of trans-oceanic large tsunamis: two events in the Pacific Ocean, namely the Tohoku tsunami with M_w 9.0 and the epicenter was located at 38.3° N and 142.4° E, occurred on

March 11, 2011 at 05:51 UTC off the east-coast of the Tohoku district, Japan and the Chile event with M_w 8.2 and the epicenter was positioned at 19.6° S and 70.8° W, occurred on April 1, 2014 at 23:47 UTC off the coast of Iquique, Chile, and other two occurrences in the Indian Ocean, namely the Aceh tsunami with M_w 9.1 and the epicenter at 3.4° N and 95.7° E, occurred on December 26, 2004 at 01:18 UTC off the west-coast of Meulaboh, Aceh, and the 2010 Mentawai tsunami with a lesser magnitude of M_w 7.7 and the epicenter at 3.5° S and 100.1° E, occurred on October 25, 2010 at 14:42 UTC off the west-coast of Mentawai island (here UTC is used for the abbreviation of Universal Time Coordinate).

For each case tsunami considered, we provided a number of numerical datasets of travel times collected from direct comparison of simulated waveforms (see Rabinovich et al. 2011; Inazu and Saito, 2013; Satake et al. 2013; Watada et al. 2014; Gusman et al. 2015) and those recorded by the monitoring DARTs and gauges managed by the National Oceanic and Atmospheric Administration (NOAA) at various geographical locations around the globe. The locations of the buoys and the gauges with the resulting observed tsunami travel times were accessed at https://www.ngdc.noaa.gov. The global bathymetry viewer was accessed at https://maps.ngdc.noaa.gov/viewers/bathymetry/ and the corresponding data was accessed at https://ngdc.noaa.gov/mgg/global/relief/ETOPO1/ for careful examinations of the complex bathymetry of the two Oceans. From the two corresponding values of travel times, both measured and predicted values, we derived paired datasets in the present study and the paired datasets allowed us to simply calculate travel time delay. The delays were then tabulated and here classified into three observational regions (see Cholifah and Prastowo, 2017), depending upon a DART or gauge location measured from the source, namely near-field, intermediate-field, and far-field zonal tsunami observations. Watada et al. (2014) and Gusman et al. (2015) argued that zones of measurements were only near-field and far-field observations but these different views gave no different qualitative results.

Following Cholifah and Prastowo (2017), we argued that near-field data were records provided by the DARTs and the gauges of less than 3,000 km away from the epicenter. Data for intermediate-field were directly obtained from the two types of instruments positioned in the ranges 3,000-12,000 km. Far-field data observations were given by monitoring stations located at a distance of more than 12,000 km away. In comparison with estimated travel times, these measured travel times led to the apparent time delay. For all cases considered in the present study, we analyzed the data for the delays, which were plotted against epicentral distance to see the nature of the delay in correspond to increasing travel distance for each case. We then analyzed different pathways and mechanisms of tsunami wave propagation between the Pacific and the Indian Ocean tsunamis and thus determined possible sources of increasing time delay in relation to tsunami speed reduction induced by geophysical disturbances during tsunami propagation. The results for all events are discussed in terms of the speed reduction, as predicted in equation (5) by Inazu and Saito (2013), as well as tsunami energy dissipation while propagating away from the source.

RESULTS AND DISCUSSION

The results for all the Pacific and Indian Ocean tsunamis considered in the present study are given in the forms of tables and corresponding graphs. Regarding apparently different characteristics of the two Oceans, we provide the 2011 Tohoku and the 2014 Chile events as the first two cases discussed then followed by the 2004 Aceh and the 2010 Mentawai tsunamis as the last two major events to discuss. Corresponding graphs for each case are generated by time delays resulted from the paired datasets of observed and predicted tsunami travel times and by epicentral distances at which the delays to occur for all observational points of view contributed from field measurements by the buoys and the gauges.

Table 1 provides a coded list of 13 DART buoys distributed over different geographical locations used in the present study, covering all zones of tsunami observations from near-field to far-field regions and resulting travel times from numerical simulations and direct observations. The apparent difference in travel time is again defined as travel time delay, which is here measured in minutes in the last column.

Table 1. The paired datasets for the 2011 Tohoku tsunami occurrence with travel time delay is calculated from the difference between observed and estimated travel times for each DART code.

DART Code	Observational Location	Latitude	Longitude	Epicentral Distance (km)	Estimated Travel Time (h)	Observed Travel Time (h)	Travel Time Delay (min)
21413	near-field	30.51° N	152.12° E	1,246	1.29	1.30	0.6
21415	near-field	50.18° N	171.85° E	2,670	3.14	3.18	2.4
52402	intermediate	11.88° N	154.12° E	3,165	3.71	3.76	3.0
52403	intermediate	4.05° N	145.59° E	3,828	4.91	4.97	3.6
46409	intermediate	55.30° N	211.48° E	5,344	6.71	6.78	4.2
52406	intermediate	5.29° S	165.00° E	5,388	6.71	6.80	5.4
51407	intermediate	19.59° N	203.41° E	6,183	7.63	7.74	6.6
51425	intermediate	9.51° S	183.76° E	6,839	8.11	8.23	7.2
46411	intermediate	39.35° N	232.98° E	7,486	9.23	9.35	7.2
43412	intermediate	16.07° N	253.00° E	10,619	13.40	13.59	11.4
51406	intermediate	8.48° S	234.97° E	10,828	13.37	13.59	13.2
32411	far-field	4.99° N	269.16° E	12,741	16.57	16.82	15.0
32412	far-field	17.97° S	273.61° E	14,816	18.90	19.18	16.8

The paired datasets listed for time delays indicate that all observed tsunami waves in nature arrive later relative to simulated tsunami waveforms from a couple of minutes to teens of minutes for further

stations. In other words, the delays in time increase with increasing epicentral distance measured from the source. This suggests that tsunami speed slows down at places far away from the epicenter. This is sensible in that at remote regions the speed predicted by equation (5) is slowed down by ~ 1% from its theoretical value given by equation (3) for the long-wave approximation. The reduction in speed is attributable to effects of variable bottom topography at seabed induced by the elasiticity of the solid Earth, as claimed by some previous work (Inazu and Saito 2013; Allgeyer and Cummins, 2014; Watada et al. 2014; Gusman et al. 2015; Wang 2015; Cholifah and Prastowo, 2017). In order to make the speed reduction clear, we here provide a plot of the time delay on increasing epicentral distance for the Tohoku case in Figure 2.

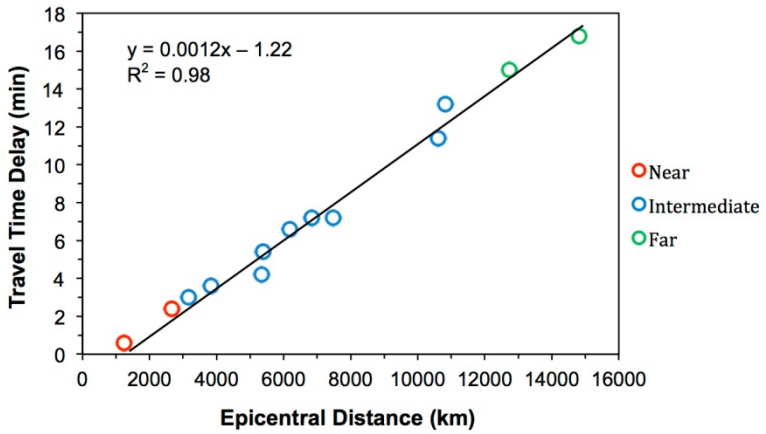

Figure 2. Travel time delay as a function of epicentral distance for the 2011 Tohoku event.

Some interesting points are made from the plot, where time delay is shown to be a linear function of epicentral distance. For total travel distances of less than 1,000 km away from the source (near-field regime) the delay is ignored, implying no apparent differences in travel times between observations and simulations. For this ignored delay, we argue that this covered travel distance is not much influenced by loading effects of the elastic Earth and thereby giving no delays in time. However, the near-field regime covers a travel distance of approximately 3,000 km away, taking a travel time of corresponding 4 hours for the Tohoku tsunami with a typical speed of 720 km/h to travel across the Pacific with small amounts of energy loss by dissipation during propagation and with no significant change in the waveforms due to insignificant geophysical disturbances (Watada, 2013; Allgeyer and Cummins, 2014; Watada et al. 2014). We found that the small speed reduction in the near-field regime (red open-circles) is associated with a small amount of the delay, which is up to 1% of the estimated travel time of the linear long-wave.

For intermediate regime shown as blue open-circles in Figure 2, in the ranges 3,000-12,000 km, the delays appear to linearly increase with travel distance, confirming that the simulated waveforms with shorter travel times are leading to the observed waves. The delays in time are found between 3.0

and 15.0 minutes, which is consistent with previous work (Allgeyer and Cummins, 2014; Watada et al. 2014). As the distance increases, effects of geopotential disturbances as predicted by equation (5) is larger on the tsunami wave, resulting in a slightly larger reduction in speed, relatively compared with equation (3). The speed reduction varies from 1.3 to 1.6%, comparable with the 1% reported tsunami speed reduction in the same region of observation (Inazu and Saito 2013; Tsai et al. 2013; Wang, 2015).

For far-field observations where the wave travels to a travel distance of more than 12,000 km or equivalent to a travel time of more than 16 hours, a further speed reduction takes place, corresponding to a longer time delay of more than 15.0 minutes, shown as two green open-circles in Figure 2. However, the longer time delays in this regime give no significant change in the proportion of the speed reduction, relative to the long-wave speed. In other words, for remote areas a value of approximately 17 minutes only corresponds to a small reduction in tsunami speed valued for about 1.5% that is comparable with that for the intermediate observations (Inazu and Saito, 2013; Tsai et al. 2013; Allgeyer and Cummins, 2014; Watada et al. 2014; Gusman et al. 2015; Cholifah and Prastowo, 2017).

As stated in the previous paragraphs, the time delays are arguably owing to the speed reduction. This reduction is associated with energy dissipation when the wave encounters geophysical perturbations during its propagation across the Pacific. It follows that the reduction in speed may relate to pathways and mechanisms of tsunami energy decay in space and time as the wave advances away from the source. We discuss this issue in details later after all events are presented for comparison.

As comparison, Table 2 below provides a total of 19 DARTs at different geographical locations, marking observational regions from near-field to far-field zones. As also with Table 1, the datasets give travel times from simulations and observations. Again, the time delay is given in minutes.

Table 2. The paired datasets for the 2014 Chilean tsunami occurrence with travel time delay is calculated from the difference between observed and estimated travel times for each DART code.

DART Code	Observational Location	Latitude	Longitude	Epicentral Distance (km)	Estimated Travel Time (h)	Observed Travel Time (h)	Travel Time Delay (min)
32401	near-field	20.47° S	73.42° W	288	0.41	0.43	0.9
32402	near-field	26.74° S	73.98° W	853	1.15	1.18	1.7
32412	near-field	17.97° S	273.61° E	1,642	2.24	2.28	2.6
32413	near-field	7.40° S	266.50° E	2,797	3.79	3.85	3.5
32411	intermediate	4.99° N	269.16° E	3,505	5.38	5.43	2.6
43412	intermediate	16.07° N	253.00° E	5,595	8.24	8.29	3.5
46412	intermediate	32.46° N	239.44° E	7,838	11.65	11.74	5.6

DART Code	Observational Location	Latitude	Longitude	Epicentral Distance (km)	Estimated Travel Time (h)	Observed Travel Time (h)	Travel Time Delay (min)
46411	intermediate	39.35° N	232.98° E	8,770	12.88	13.00	7.1
51426	intermediate	22.99° S	191.87° E	9,869	13.68	13.78	6.5
51407	intermediate	19.59° N	203.41° E	10,301	13.96	14.09	8.0
46409	intermediate	55.30° N	211.49° E	11,036	16.18	16.35	10.6
46402	intermediate	51.07° N	195.98° E	11,904	16.59	16.76	10.6
21414	far-field	48.97° N	178.22° E	13,147	17.76	17.96	11.5
52406	far-field	5.29° S	165.00° E	13,304	18.53	18.71	10.6
21419	far-field	44.46° N	155.74° E	14,916	19.65	19.88	14.1
52401	far-field	19.26° N	155.77° E	15,134	20.35	20.55	11.8
52402	far-field	11.88° N	154.12° E	15,143	20.21	20.42	12.7
21418	far-field	38.71° N	148.69° E	15,660	20.42	20.67	14.9
52405	far-field	12.88° N	132.33° E	17,443	23.63	23.91	16.6

In general, the content of Table 2 is similar to that of Table 1. It follows that the behavior of tsunami propagation in the Pacific is independent of the propagation direction, whether the wave travels from the west Pacific to the east as in the Tohoku or on the other way around as in the Iquique tsunami. From the datasets provided in Table 2, we can examine that all time delays are due to the late arrivals of the observed waves detected at all nearby and far stations. The delays for the 2014 Iquique tsunami are in the ranges 10.6-16.6 minutes for far-field, comparable with 15 minutes of delay for the same regime of observation (Heidarzadeh et al. 2014). This trend in minutes of delay tends to be similar to that for the Tohoku case, implying that the speed reduction is similar for the Tohoku and Iquique tsunamis during tsunami propagation across the Pacific. Whereas Gusman et al. (2015) addressed the delays for distant propagation recorded by far-field stations at a longer travel time by 1-2% compared with predicted travel time, we claim the same amount of proportion for the speed reduction (see, for the 2011 Tohoku event, Cholifah and Prastowo, 2017). All delayed signals observed by DARTs for the Pacific tsunamis were found to correspond to β given in equation (5), introduced as variations in bottom topography (Inazu and Saito, 2013). For direct comparison, we here plot the time delay against epicentral distance for the 2014 Iquique event in Figure 3 below.

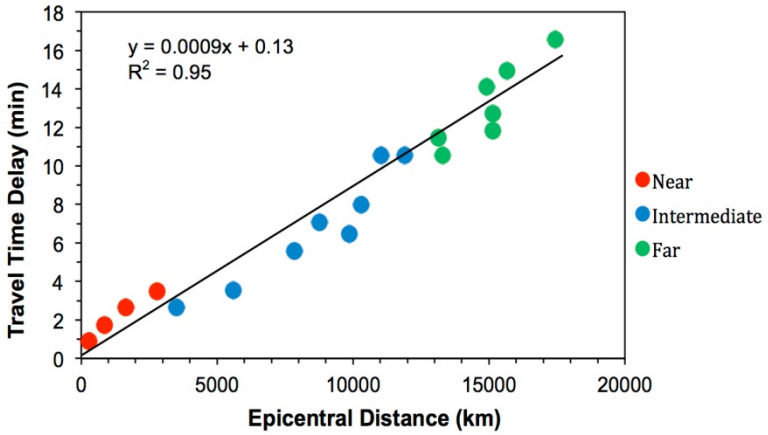

Figure 3. Travel time delay as a function of epicentral distance for the 2014 Chilean event.

Again we have time delay to be a linear function of travel distance for the 2014 Chilean event. For travel distances of less than 1,000 km in the near-field zone the delay remained less than 2 minutes, considered unimportant for tsunami early warnings. This ignored influence of the Earth elasticity effects upon the speed reduction goes further to only a short travel distance of about 1,500 km away, where topographical effects started to reduce the speed. With almost the same speed as in the case of the 2011 Tohoku tsunami, the loss in energy during propagation of the 2014 Iquique event in this field is only responsible for a small amount of the time delay (Gusman et al. 2015), accounted for about 1.5% of the estimated travel time calculated using the long-wave speed. For the intermediate and far regimes of observations, the time delays appear to linearly increase with increasing travel distance, again confirming similar behaviors of tsunami propagation in the Pacific. The maximum delay in the present study is up to 16.6 minutes achieved at a region of radius 17,500 km away from the source, close to the 15 minute-late arrivals of the observed waves reported by Heidarzadeh et al. (2014) for the Iquique event. This finding is also consistent with the maximum delay of 16.8 minutes for roughly the same distance in the 2011 event although the reasons for the delays reported by Cholifah and Prastowo (2017) did not include factors, such as seawater compressibility and geopotential variation, which may also be important for variations in tsunami speed in remote propagation. The point to make here is that a 1-2% speed reduction is found in the Pacific tsunamis, consistent with previous studies (Inazu and Saito, 2013; Tsai et al. 2013; Allgeyer and Cummins, 2014; Watada et al. 2014; Gusman et al. 2015).

For a complete examination, we provide in Table 3 below a number of tide-gauge stations at different locations in the Indian Ocean territory, listing observed and estimated travel times and hence time delay for each monitoring instruments used. Due to its complexity induced by complex bathymetry and different routes of tsunami propagation direction across the Indian Ocean (Rabinovich et al. 2011), we here only provide 5 paired datasets from tide-gauge field measurements, covering to only near-field and intermediate regimes of observations.

Table 3. The paired datasets for the 2004 Aceh tsunami occurrence with travel time delay is calculated from the difference between observed and estimated travel times for each tide-gauge station.

Tide Gauge	Observational Location	Latitude	Longitude	Epicentral Distance (km)	Estimated Travel Time (h)	Observed Travel Time (h)	Travel Time Delay (min)
Chennai	near-field	13.04° N	80.17° E	2,011	2.57	2.60	2.0
Male	near-field	4.18° N	73.52° E	2,441	3.25	3.42	10.0
Garcia	near-field	7.28° S	72.40° E	2,819	3.77	3.92	9.0
La Rue	intermediate	4.57° S	55.53° E	4,505	7.28	7.42	8.0
Lamu	intermediate	2.27° S	40.90° E	6,060	8.88	9.15	16.0

The results for the Indian Ocean tsunami show somewhat but clear difference in trend between increasing travel distance and its corresponding delays (see for example, gauge stations at Male, Garcia, and La Rue). These three stations measured a step decrease in the delay as travel distance increases, raising a question of whether the delay is a linear function of epicentral distance remains applicable for this case. However, the overall assessment derived from examination of signals arrived at Chennai, India, then one of the three stations at Male (Maldive islands), Diego Garcia, and Pointe La Rue in the open Indian Ocean up to Lamu observatory in the northern of Zanzibar (at the far east coast of Africa mainland) indicates a linearly positive correlation between time delay and epicentral distance for the 2004 event. What makes remarkably interesting here is that a maximum of 16.0 minute delay in this case was found for a much shorter travel distance, only at about 6,000 km away (the waves in the 2011 and 2014 events achieved approximately the same amount of such a time delay for more than doubled travel distance). Considering different properties of the Pacific and Indian Oceans, we speculate that this is an indicative of different tsunami pathways and mechanisms of propagation between the trans-Pacific tsunamis (the 2011 Tohoku and the 2014 Iquique occurrences) on one hand and the Indian Ocean tsunamis (the 2004 Aceh and the 2010 Mentawai events) on the other hand. To analyze further the distinguished characteristics between the two trans-oceanic tsunamis, we plot in Figure 4 (although with only limited points) time delay against travel distance for the 2004 Aceh event.

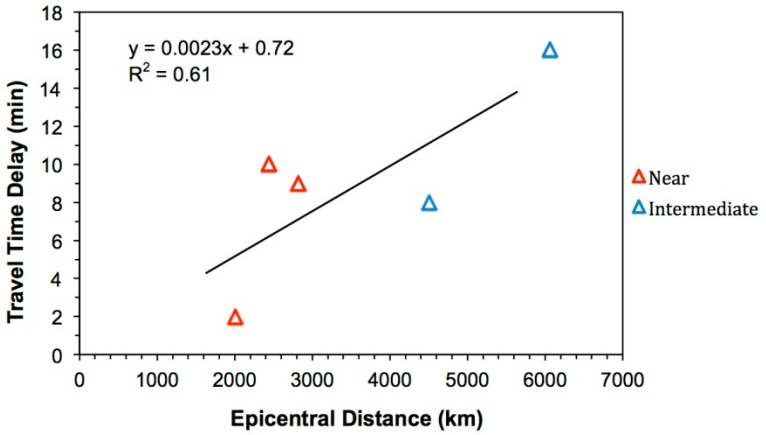

Figure 4. Travel time delay as a function of epicentral distance for the 2004 Aceh event.

Careful analysis of the determination coefficient represented by R^2 values and the slopes of lines of regression for each event from Figures 2, 3, and 4 reveal good arguments for the discrepancy in trend of time delay particularly for the Pacific and Indian Ocean tsunamis. In the case of the Pacific events, R^2 is found to be 0.98 for the 2011 Tohoku and 0.95 for the 2014 Iquique, providing a clear clue that dynamics of tsunamis in the Pacific is similar, independent of propagation direction and other regional perturbations owing to similar propagation characteristics. Thus, for a relatively large value of $R^2 \approx 1$ in the Pacific case, the delay is a remarkable linear function of travel distance measured from the source. The similar linear dependence of travel time delay on epicentral distance for the trans-Pacific tsunamis also indicates that the waves propagate along the same semi-enclosed ocean basin with the same level of roughness of bathymetry and that during the same amount of travel time they distribute the energy over long distances and dissipate it in the same fundamental mechanism of sea bottom friction along tsunami flow advection. Another interesting feature from Figures 2 and 3 to discuss is that the slopes in two regression lines are comparable, where they are rounded to 0.001 to three decimal places (within the considered unimportant errors of 0.0002 in all points from the near-field to the far-field for the 2011 Tohoku and the 2014 Iquique).

In contrast to the Pacific events, the data for the 2004 Aceh tsunami in the Indian Ocean show more scattered datapoints with a much smaller value of $R^2 = 0.61$ but this is in fact in good agreement with $R^2 = 0.59$ taken from "the west route" recorded by a network of coastal and mainland observatories discussed in the work of Rabinovich et al. (2011). Considering this primary finding in relation to Figure 4, we can say, to some extent, that the time delay is longer for a further travel distance but there is unlikely linear relationship between the delay and the epicentral distance for this case. We also find that the slope of the regression line for the 2004 Aceh tsunami is 0.002 (rounded to three decimal places), implying that the 2004 tsunami reached the same amount of time delay as the other two events in the Pacific Ocean but within a shorter distance, almost a half of that taken by the trans-Pacific tsunamis. The possible cause for this remarkable delay difference is that the Indian

Ocean is poorly understood with the more complex bathymetry and coarse topography along the direction line of tsunami propagation relatively compared with the Pacific Ocean, as implied by the works of Rabinovich et al. (2011, 2013). Another possible cause for the clear difference in the delays between the Pacific and the Indian Ocean tsunamis seems due to different mechanisms of energy decay. While advection dominates over diffusion in the Pacific in which the energy is dissipated in a rate that is much slower than that in the Indian Ocean, as also implied by Prastowo et al. (2017), the two mechanisms are in balance for the 2004 Aceh tsunami such that the loss of energy is controlled by both advection and diffusion effects.

Within the framework of a hypothetical strong influence of diffusion upon the speed reduction in the Indian Ocean tsunami, we here provide one more case study of another tsunami event that occurred in this region for a further clarification whether diffusion effects play a role in dissipating the energy and hence reducing the speed. Below is Table 4, consisting of datasets for the 2010 Mentawai case, where the data were obtained from field surveys (see Satake et al. 2013).

Table 4. The paired datasets for the 2010 Mentawai tsunami occurrence with travel time delay is calculated from the difference between observed and estimated travel times for each tide-gauge station.

Tide Gauge	Observational Location	Latitude	Longitude	Epicentral Distance (km)	Estimated Travel Time (min)	Observed Travel Time (min)	Travel Time Delay (min)
Padang	near-field	0.95° S	100.36° E	280	66.66	68.33	1.7
Tlk. Dalam	near-field	0.33° N	97.49° E	509	61.66	63.33	1.7
Cocos	near-field	12.11° S	96.89° E	1,013	81.66	81.86	0.2
Colombo	near-field	6.57° N	79.50° E	2,522	242.22	245.55	3.3
D. Garcia	intermediate	7.28° S	72.40° E	3,077	245.71	247.14	1.4
Rodrigues	intermediate	19.68° S	63.42° E	4,412	356.25	360.00	3.8
La Rue	intermediate	4.66° S	55.53° E	4,906	472.77	476.66	3.9
Port Louis	intermediate	20.15° S	57.50° E	5,033	432.50	442.50	10.0

The results for the 2010 Mentawai event in the Indian Ocean seem to have a similar behavior to those for the 2004 Aceh tsunami. The similarity of the two events can be concluded from the scatter of the data presented in Table 4. A relatively small amount of delay in time of only 0.2 minutes recorded by the Cocos-island observatory is likely due to its geographical location with respect to the source, where the island is directly positioned along the main path of tsunami energy distribution. As is the case for other events, travel time delay increases with travel distance for the 2010 Mentawai event (see, for example, Cholifah and Prastowo, 2017) owing to the Earth elastic loading in particular

for distant propagation (see, for example, Inazu and Saito, 2013; Watada et al. 2014). However, there remains a question about the nature of the time delay in the sense that whether the delay is a linear function of increasing epicentral distance. To clarify this issue, we plot in Figure 5 time delay against travel distance for the 2010 Mentawai event.

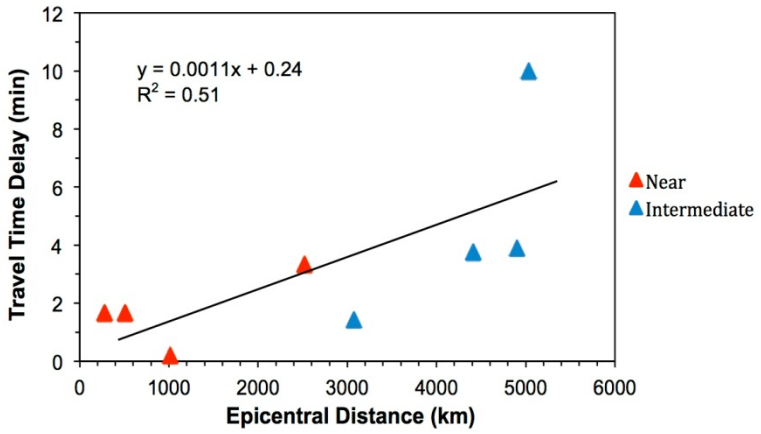

Figure 5. Travel time delay as a function of epicentral distance for the 2010 Mentawai event.

There is an interesting point to discuss from Figure 5. Noticeably, a value of $R^2 = 0.51$ was found for the 2010 Mentawai tsunami, comparable with that for the 2004 Aceh event (see Figure 4), indicating a similar behavior of tsunami propagation for both events. This is sensible because the two events were to occur in nearby regions off the west-coast of Sumatra with almost the same route for tsunami propagation across the Indian Ocean (see e.g., Rabinovich et al. 2011). Because a R^2 value is a statistical measure of the linearity of a given regression line, the relatively small values of R^2 for the Aceh and the Mentawai tsunamis confirm that the time delays in both events are not a linear function of increasing travel distance. It follows that relatively compared with the trans-Pacific tsunamis, the propagation of tsunami waves with the epicenters in the Indian Ocean is much affected by complicated sea bottom topography. As discussed by Prastowo et al. (2017) using a speed parameter of c/c_s where c is the theoretical long-wave speed and c_s is the complex speed (consisting of advection and diffusion components) applied to the 2010 Mentawai event, they showed that diffusion cannot be ignored in particular regions of the Indian Ocean. In this way, the rate of tsunami energy dissipation by horizontal flow advection and ocean diffusion for tsunami waves across the Indian Ocean is relatively higher than that for the trans-Pacific tsunamis. This argument is supported by the data in Tables 1 and 2 for the Pacific events compared with those in Tables 3 and 4 for the Indian Ocean tsunamis, where the same amount of time delay of ranging from 10 to 17 minutes is attained in a much shorter travel distance for tsunami waves that traveled in the Indian Ocean than those propagated in the Pacific.

Using a huge number of data for travel times from the Pacific and Indian Oceans, Wessel (2009) reported a significant departure of recorded travel times from predicted values of the linear long-wave theory. Although topographic disturbances were suspected as the possible cause for the late arrivals of the observed waves, he did not say about the speed reduction as the candidate for the corresponding travel time delay. There came about in several years later (see Tsai et al. 2013; Watada, 2013), where most of scientists started to realize that tsunami phase speed varies with both the internal factors, such as that given by seawater density variability and the external factors, such as that given by the dynamics of the elastic Earth in the form of seafloor deformation. In a careful examination using tsunami model of propagation for trans-Pacific tsunamis under influenced by effects of elastic loading, Watada et al. (2014) concluded that the observed speed could be reduced to 98% of the predicted the linear long-wave speed. It follows that the reduction in speed for the trans-Pacific tsunamis under consideration is of up to 2%. This magnitude of reduction is comparable with our findings of up to 3% reduction (including the 2004 Aceh and the 2010 Mentawai events) estimated from travel time delay in each case study (see Tables 1 and 2 for the Pacific events and Tables 3 and 4 for the Indian Ocean tsunamis). Using the field data for the Pacific occurrences as a reference for its linearity of time delays with respect to epicentral distances, we find that a 1-2% reduction in speed corresponds to $\beta = 0.02$-0.04 in this study, in good agreement with $\beta = 0.015$-0.020 reported by Inazu and Saito (2013) and further clarified by computational studies using additional effects of seawater compressibility and density variation in the ocean stratification (Allgeyer and Cummins, 2014; Watada et al. 2014; Gusman et al. 2015; Wang, 2015).

Other factors that may affect tsunami wave propagation in the open ocean include wave behavior, such as wave dispersion. Using the so-called “dispersion time” as the only single parameter examined in their computational work (Glimsdal et al. 2013), they claimed that the frequency-dependent speed is proved to be important for dispersive tsunamis especially in remote regions away from the source. This parameter is used to measure the effect of dispersion during tsunami propagation. For tsunamis of seismic origin with moderate magnitudes, the dispersion time was found relatively larger. It follows that these earthquakes may generate tsunami waves with frequency-dependent speed for all regimes of observations. However, for large tsunamigenic earthquakes this effect plays a role in reducing the speed for only at distant observations (Glimsdal et al. 2013). Although they did not relate their results to travel time delay, the consequence of the relative importance of dispersion effects on tsunami speed is clear in that the difference in tsunami speed between observations and simulations exists for particularly distant propagation. At this point, we could say that our findings in the case of the trans-Pacific tsunamis where a systematic linear increase in travel time delay against increasing travel distance are consistent with the work of Glimsdal et al. (2013). As travel distance increases, we speculate that the wave energy decays in time via dissipation due to advection, diffusion, and dispersion but this paper does not discuss these effects. Instead, this study focuses on analyzing travel time delay in relation to speed reduction.

The results for all regions of space for field monitoring of the Pacific and Indian Ocean tsunamis considered in the current study show surprising findings in the sense that while the time delay taken up by the computed and observed waves increases linearly for the case of the Pacific events, the proportion of the reduced speed is fixed with the speed reduction is valued between 1.0-1.6%, in good agreement with previous studies (Inazu and Saito, 2013; Tsai et al. 2013; Allgeyer and Cummins, 2014; Watada et al. 2014; Gusman et al. 2015; Cholifah and Prastowo, 2017). We believe that to some extent the qualitative results are independent of either the precise observations by the field monitoring instruments or the accuracy in predicted travel times by the numerical simulations. An improved numerical model of tsunami propagation by incorporating additional effects, such as compressibility of seawater upon the vertical stratification of the density field into the equations of motion, as suggested by Watada (2013), is therefore necessary for a better correction of the delays. It should be noted that there are at least two logical consequences that can be drawn from these findings. Firstly, it is true to conclude that tsunami speed varies primarily with the external parameters, such as effects of the complex bathymetry and the local topography induced by the elasticity of the solid Earth in the form of seafloor deformation on the non-rigid bottom topography (Allgeyer and Cummins, 2014; Watada et al. 2014; Gusman et al. 2015). Secondly, the speed reduction indicates that tsunami energy is lost due to dissipation by both advective flow of a tsunami wave and oceanic diffusion. The loss of energy, specified as energy decay in space and time during propagation in the Indian Ocean as discussed by Rabinovich et al. (2011) and in the Pacific as further investigated by Rabinovich et al. (2013), needs clarifying regarding estimates of energy dissipation in compressible fluids that go beyond of this study and therefore this issue, along with the inclusion of seawater compressibility in the equations of motion, is promising for future work.

3. CONCLUSIONS

Travel time delay for trans-oceanic tsunamis across the Pacific and Indian Oceans has been analyzed using paired datasets from simulated waveforms and field records from the DARTs and gauges. In this study, travel time estimates for the 2011 Tohoku, the 2014 Chilean, the 2004 Aceh, and the 2010 Mentawai events were compared with travel times from field records. Particularly for the Pacific tsunamis, the time delay is found to linearly increase with epicentral distance, suggesting that the speed is reduced during propagation. From careful analyses of the time delays, we conclude that the reduction in speed in the Pacific Ocean is 1-2% from the long-wave speed but it is twice or larger in the Indian Ocean owing to its complexity. For far-field propagation of more than 15,000 km in the Pacific, the time delays could be of up to 17 minutes while the same amount of travel time delay was achieved at a much shorter distance in the Indian Ocean.

Regarding the results for the Indian Ocean, where most coastal regions in the Sunda-arc islands within the Indonesian territories are vulnerable to geophysical hazards, including destructive tsunamis a number of more sensitive monitoring instruments are needed to detect the generation and propagation of a tsunami wave in the Ocean, and its arrival nearby and at shorelines. Therefore, near-

field and far-field tsunami observations are required for better tsunami detection and disaster preparedness with the help of improved travel time forecast. Within the context of mitigation study, knowledge of accurate time delay is thus important for tsunami early warning to minimize potential losses of buildings, properties, and lives. This can be possibly achieved by rapid analyses of tsunamigenic earthquakes and accurate prediction of arrival times hence time delays recorded at a network of regional stations.

Acknowledgements

The authors would like to thank anonymous reviewers for their best suggestions and invaluable comments upon this article from its simple form of an originally submitted version to a form of a high level quality required for publication in STH.

References

Allgeyer, S. and P. Cummins (2014), Numerical tsunami simulation including elastic loading and seawater density stratification, Geophys. Res. Lett., 41, 2368-2375, doi:10.1002/2014GL059348.

Cholifah, L. and T. Prastowo (2017), Travel time difference between estimated and observed values of the 2011 trans-oceanic Tohoku tsunami, Proc. 7th Basic Science International Conference (BaSIC), Malang: Faculty of Science, The University of Brawijaya.

Fine, I. V., E. A. Kulikov and J. Y. Cherniawsky (2013), Japan's 2011 tsunami: characteristics of wave propagation from observations and numerical modeling, Pure Appl. Geophys., doi:10.1007/s00024-012-0555-8.

Glimsdal, S., G. K. Pedersen, C. B. Harbitz and F. Løvholt (2013), Dispersion of tsunamis: does it really matter? Nat. Hazards Earth Syst. Sci., 13, 1507-1523, doi:10.5194/nhess-13-1507-2013.

Gusman, A. R., S. Murotani, K. Satake, M. Heidarzadeh, E. Gunawan, S. Watada and B. Schurr (2015), Fault slip distribution of the 2014 Iquique, Chile, earthquake estimated from ocean-wide tsunami waveforms and GPS data, Geophys. Res. Lett., 42, 1053-1060, doi:10.1002/2014GL062604.

Heidarzadeh, M., K. Satake, S. Murotani, A. R. Gusman and S. Watada (2014), Deep-water characteristics of the trans-Pacific tsunami from the 1 April 2014 Mw 8.2 Iquique, Chili earthquake, Pure Appl. Geophys., doi:10.1007/s00024-014-0983-8.

Inazu, D. and T. Saito (2013), Simulation of distant tsunami propagation with a radial loading deformation effect, Earth Planets Space, 65, 835-842, doi:10.5047/eps.2013.03.010.

Prastowo, T., L. Cholifah, L. O. Ngkoimani and L. O. Safiuddin (2017), Tsunami-magnetic signals and magnetic anomaly generated by tsunami wave propagation at open seas, Jurnal Pendidikan Fisika Indonesia, 13(1), 59-70.

Prastowo, T. and T. N. Ain (2015), Experiments on gravity current to examine concepts of hydrodynamics and mass conservation for incompressible fluids, Jurnal Pendidikan Fisika Indonesia, 11(1), 84-92.

Rabinovich, A. B., R. N. Candella and R. E. Thomson (2011), Energy decay of the 2004 Sumatra tsunami in the world ocean, Pure Appl. Geophys., 168, 1919-1950, doi:10.1007/s00024-011-0279-1.

Rabinovich, A. B., R. N. Candella and R. E. Thomson (2013), The open ocean energy decay of three recent trans-Pacific tsunamic, Geophys. Res. Lett., 40, 3157-3162, doi:10.1002/grl.50625.

Satake, K., Y. Nishimura, P. S. Putra, A. R. Gusman, H. Sunendar, Y. Fuji, Y. Tanioka, H. Latief and E. Yulianto (2013), Tsunami source of the 2010 Mentawai, Indonesia earthquake inferred from tsunami field survey and waveform modeling, Pure Appl. Geophys., 170, 1567-1582, doi:10.1007/s00024-012-0536-y.

Suppasri, A., K. Goto, A. Muhari, P. Ranasinghe, M. Riyaz, M. Affan, E. Mas, M. Yasuda and F. Imamura (2015), A decade after the 2004 Indian Ocean tsunami: the progress in disaster preparedness and future challenges in Indonesia, Sri Lanka, Thailand, the Maldives, Pure Appl. Geophys., 172, 3313-3341, doi:10.1007/s00024-015-1134-6.

Tsai, V. C., J. P. Ampuero, H. Kanamori and D. J. Stevenson (2013), Estimating the effect of earth elasticity and variable water density on tsunami speeds, Geophys. Res. Lett., 40, 492-496, doi:10.1002/grl.50147.

Wang, D. (2015), An ocean depth-correction method for reducing model errors in tsunami travel time: application to the 2010 Chile and 2011 Tohoku tsunamis, Sci. Tsunami Hazards, 34(1), 1-22.

Watada, S. (2013), Tsunami speed variations in density-stratified compressible global oceans, Geophys. Res. Lett., 40, 4001-4006, doi:10.1002/grl.50785.

Watada, S., S. Kusumoto and K. Satake (2014), Traveltime delay and initial phase reversal of distant tsunamis coupled with the self-gravitating elastic earth, J. Geophys. Res., 119, 4287-4310, doi:10.1002/2013JB010841.

Wessel, P. (2009), Analysis of observed and predicted tsunami travel times for the Pacific and Indian oceans, Pure Appl. Geophys., 166, 301-324, doi:10.1007/s00024-008-0437-2.

ISSN 8755-6839

SCIENCE OF **TSUNAMI HAZARDS**

Journal of Tsunami Society International

Volume 37 **Number 4** **2018**

TSUNAMI DANGER IN THE KERCH STRAIT

R.Kh. Mazova, E.A. Baranova, Yu.G. Belov, Yu.I. Molev, S.M. Nikulin, V.D. Kuzin

Nizhny Novgorod State Technical University n.a. R.E. Alekseev, 24, Minin st., 603095 Nizhny Novgorod, Russia

ABSTRACT

The numerical simulation of the tsunami wave propagation along the Kerch Strait is carried out with localization of possible sources at the entrances to the strait, both from the Black Sea and from the Sea of Azov. Under computation of both generation and tsunami propagation, a system of nonlinear shallow water equations was used. The potential strong earthquakes (with earthquake magnitude M ~ 7) with seismic sources of elliptical shape were considered. Detailed assessments of the wave characteristics in the Kerch Strait, in particular for the Crimean bridge area, were carried out. The obtained wave characteristics are compared with the available data of the work of other authors.

***Key words*:** earthquake source, tsunami waves, numerical simulation, spectral characteristics of the wave field.

1. INTRODUCTION

As known, the Kerch Strait divides the Kerch Peninsula of the Crimea and the Taman Peninsula of continental Russia. On the other hand, it connects the water areas of the Black and Azov Seas, so that the Sea of Azov, as a relatively small water basin, can in fact be considered as a gulf of the Black Sea. It should be noted that the geological conditions in the Kerch Strait are quite complex - seismicity, tectonic fracture, weak soils. According to hydrogeologists, the Kerch Strait is in fact a place of a tectonic fault, and the Kerch and Taman coasts belong to different tectonic plates. Moreover, in addition to taking into account the possibility of an earthquake in the Kerch Strait itself, it is necessary to take into account the possibility of the appearance of tsunami waves coming from both the Black Sea and the Sea of Azov.

Such the tsunami was recorded on September 11-12, 1927, December 28, 1939 and July 12, 1966, when waves from the Black Sea to the Sea of Azov crossed the Kerch Strait. The echoes of these tsunamis were recorded in a number of points in the Azov Sea [1]. In general, oscillations in the water level in the Kerch Strait are of a different nature, the most significant in magnitude are the surge oscillations [2], which are also characteristic of the Sea of Azov (mini-tsunami). In the southeast of the Sea of Azov in 1969, on October 28, a tsunami struck a five-meter high water wall into the southeastern part of the sea. In 1971, such an event, but on a large scale, was repeated for the same part of the Azov Sea [3]. The tsunami of seismogenic nature in the Sea of Azov is little known [4].

Epicenters of historical relatively weak underwater earthquakes are concentrated in the southern and southwestern parts of the Azov Sea [3 – 6]. The issue of tsunami hazard research in the Black Sea and the Sea of Azov adjoining the Kerch Strait has been given attention in a number of works (see, for example, [4, 6 – 9].) Thus, in [7] a numerical analysis of tsunami wave propagation in the Azov Sea was performed. As noted in this paper, "the issue of the effectiveness of tsunami generation in the Sea of Azov by seismic sources remains relevant and little studied." These issues are now very important in connection with the beginning exploitation of the bridge across the Kerch Strait - the Crimean bridge, the automobile part of which was only recently opened, in May 2018.

In the present work, the tsunami wave propagation through the Kerch Strait is numerically simulated during the localization of possible earthquake sources at the entrances to the strait, both from the Black Sea and from the Sea of Azov. The potential strong earthquakes (with earthquake magnitude M ~ 7) with seismic source of elliptical shape were considered. The real bathymetry of the relief of the bottom of the Kerch Strait, which has a rather complex structure, is used - the transverse profile of the channel of the strait is asymmetric, and the strait itself is delimited by two spits into three parts [10]. Detailed assessments of wave characteristics in the Kerch Strait, in particular for the Crimean bridge area, were carried out.

2. NUMERICAL SIMULATION

As noted in [5], the southern section of the Crimean Peninsula's shelf is one of the most probable zones of seismic generation of tsunamis in the Black Sea. According to [5], it is impossible to exclude the possibility of underwater earthquakes with magnitudes M = 7, 0-7, 5, which can be accompanied by strong tsunami. Since one of the most probable zones of seismic generation of tsunami in the Black Sea is the southern part of the Crimean Peninsula [5], the localization of the seismic source in the Black Sea in front of the Kerch Strait to the northeast of the Crimean Peninsula (Scenario 1) (Fig. 1), and for Scenario 2 (compare [7]) - before entering the Kerch Strait from the Azov Sea side (Fig. 3).

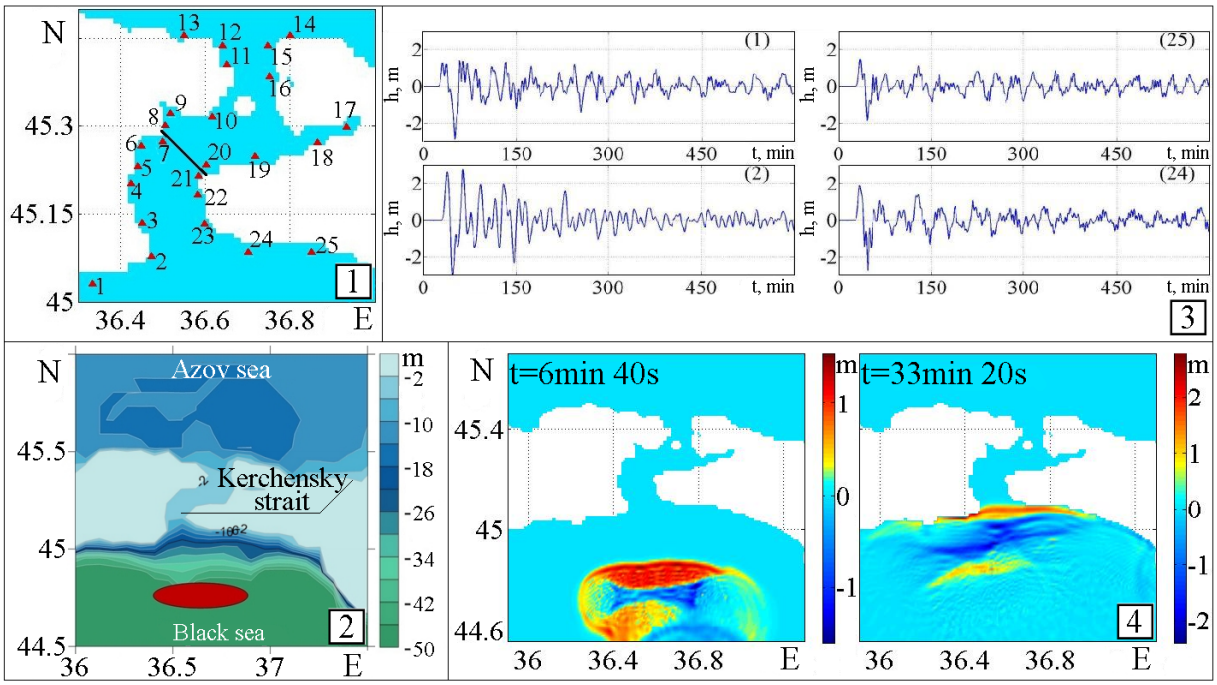

Fig. 1. Schematic representation of the water area of the Kerch Strait and the characteristics of wave fields; in the inset (1): the scheme of the virtual tide gauges along the western and eastern coasts of the Kerch Strait; in the inset (2): the location of the calculated source of the earthquake for Scenario 1; in the inset (3): data from 4 virtual gauges at the entrance to the Kerch Strait from the Black Sea (in the upper right corner there is a virtual tide gauge number): (1) - p. Yakovenkovo, (2) - p. Treasured, (24) - p. The wave, (25) - p. Artyushchenko; in the inset (4): the position of tsunami wave fronts for two time instants.

To simulate possible strong earthquakes with a magnitude of 7, we chose two hypothetical sources of an earthquake, an ellipsoidal shape with dimensions of about 16.4 x 68 km [11]. A nonlinear system of shallow water equations in a two-dimensional formulation (see, for example, [12, 13]) was used to describe the process of generation and propagation of a wave caused by the displacement of seafloor areas in the earthquake source, taking into account dissipative effects and bottom friction. In the

numerical solution, we used a scheme constructed by analogy with the scheme in [14]. The design area used for these calculations was selected in a square of 35^0-38^0 (E), 44.5^0-47.5^0 (N), with a grid including the number of nodes 345x361 = 124,545. Black Sea bathymetry with a resolution of 500 m was used for numerical simulation. The simulation was performed with a time step of 1 s [13]. In the last seaward point at a depth of 3 m, the condition of total reflection (vertical wall) is set, allowing to fix at this depth the maximum and minimum values of the shift of the wave level.

In numerical simulation, displacement wave fields and velocity fields were obtained along the northwestern coast of the Black Sea, the coasts of the Azov Sea and along the coasts of the Kerch Strait. The computation area and the layout of the virtual tide gauges along the western and eastern coasts of the Kerch Strait are shown in Fig. 1.1, 1.2. In Fig. 1.3 and Fig. 1.4 there are presented the results of numerical simulation calculations for part of the Black Sea in front of the Kerch Strait. Figure 1.3 shows the computed tide gauge records for points 1, 2, 24 and 25, located at the entrance to the strait (see Fig.1.1). It can be seen that the maximum spread in sea level oscillations in these points is almost 5 m: from +2.3 m to -2.5 m.

Figure 2 shows a picture of the propagation of a tsunami wave along the Kerch Strait. When the wave moves in the Kerch Strait, the wave height decreases and the maximum value of the height of the leading edge of the wave becomes in the the order of 1 m. With further motion of the wave, its front after 1 h 10 min reaches first the right support of the bridge, while the maximum wave height remains on the order of 1 m. After 10 minutes, the wave reaches the left support of the bridge with the wave height about 0.7 m. As can be seen from Fig. 2.3 (t = 1h), the leading edge of the elevation wave has a convex, arcuate shape across the entire width of the strait. The height of the crest in the strait, an hour after the start of the event, reaches a meter and a half.

After 1 hour and 12 minutes, the right edge of the wave front with a height of up to 0.7 m (see point 20 in Fig.2.2.) reaches the eastern bridge supports in the area of the Tuzla spit. The rest of the front continues to spread northward and after 8 minutes attacks the northern coast of Kamysh-Burun Bay and reaches west bridge supports. The height of the wave crest in point 7 (Fig.2.2) is of the order of 0.7 m. After passing the Tuzla spit, the height of the right half of the wave front is almost halved and the wave front is turned towards the Taman Bay (Fig. 2.3, t = 1h 20min). After 1 hour 30 minutes, the middle part of the wave front extends toward the northern coast of the Kerch Bay and reaches it in 10 minutes with a height of about 1 m, t = 1h 20min). At the rest of the bay the runup is about 0.5 m in height. In the vicinity of the bridge, a decrease in the water level by about 1 m is observed at this time. After 15 minutes (Fig. 2.3, t = 1h 46min 40s), a wave crest consisting of two parts approaches the bridge. The center of the bridge is subjected to the attack of a crest of a wave having a pointed shape, precisely in the area of the Tuzla spit, where the eastern pillars of the bridge are located. Another section of the wave front attacks the bridge supports at the site of its bend in the area of the Ak-Burun Cape. At the same time, the wave forefront reaches the Chushka spit, but the height of the crest is less

than 0.5 m. Approximately 2 hours 30 minutes after the tsunami generation, the Tuzla spit area (Fig. 2.3) is again attacked by waves with a crest height of more than 1 m (Fig. 2.3, t = 2h 33min 20s).

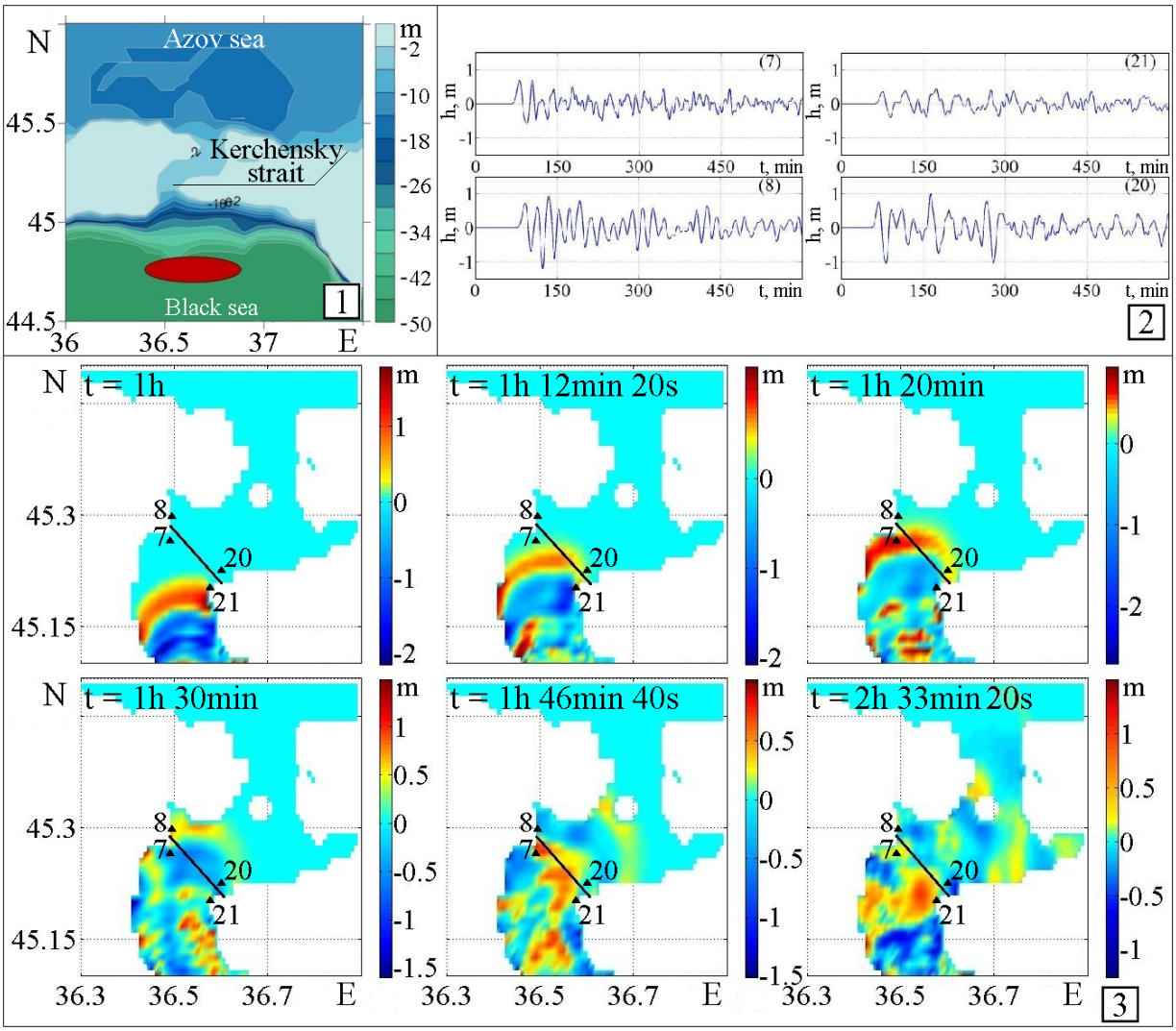

Fig. 2. Characteristics of wave fields in the Kerch Strait basin for Scenario 1; in the inset (1): the location of the calculated source of the earthquake for Scenario 1; in the inset (2): data from 4 virtual tide gauges along the Kerch Strait; (7) - left south edge of the bridge, (8) - left north edge of the bridge, (20) - right north edge of the bridge, (21) - right south edge of the bridge. In the upper right corner is the number of the virtual tide gauge; in the inset (3): the position of the tsunami wave fronts and the distribution of the water level in the Kerch Strait basin for six time moments for Scenario 1. The dark line is a schematic representation of the position of the Crimean bridge.

In the case of the implementation of Scenario 2, the picture of the propagating of a tsunami wave along the Kerch Strait is shown in Fig. 3.1. Unlike Scenario 1, the leading edge of the elevation wave after entering the strait and passing the Chushka spit is flat (Fig.3.3). The height of the crest in the strait, one hour after the beginning of the event, reaches about a meter (Fig. 3.2).

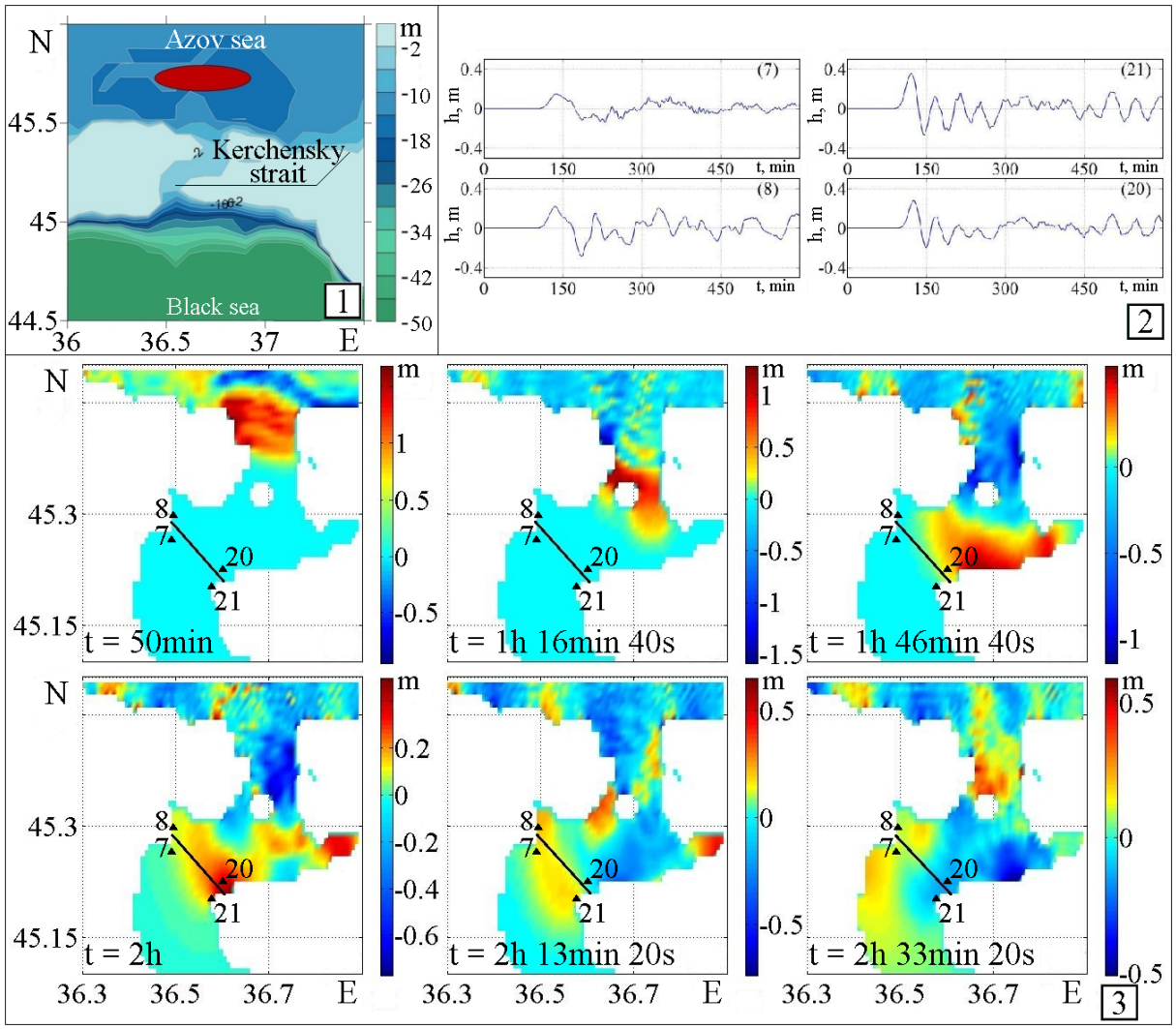

Fig. 3. Characteristics of wave fields in the basin of the Kerch Strait for Scenario 2; in the inset (1): the location of the calculated source of the earthquake for Scenario 2; in the inset (2): data from 4 virtual gauges along the Kerch Strait for Scenario 2; (7) - left south edge of the bridge, (8) - left north edge of the bridge, (20) - right north edge of the bridge, (21) - right south edge of the bridge. In the upper right corner is the number of the virtual tide gauge; in the inset (3): the position of the tsunami wave fronts and the distribution of the water level in the Kerch Strait basin for six time moments for Scenario 2. The dark line is a schematic representation of the position of the Crimean bridge.

After 1 hour and 46 minutes, the wave front reaches the southern coast of the Taman Bay with a crest height of up to half a meter in the Taman region, and also reaches the bridge supports in the Tuzla spit area (see the tide gauge records in points 20 and 21 in Fig.3.2) with wave height up to 0.4 m (Fig.3.3). The rest of the front continues to spread in the south-west direction, reaching the northern coast of the Kerch Bay. Two hours after the generation of the tsunami, the wave front reaches the bridge supports (see the tide gauge records in points 7, 8 and 20, 21 in Fig.3.2) along its entire length and enters the Kerch Bay (Fig.3.3). The wave height reaches 0.4 m in the area of the Tuzla spit, decreasing to 0.2 m near the cape of Ak-Burun. After 15min the wave passes through the bridge, remaining only in the water area of the Kerch Bay.

With further propagation, the wave front becomes more flat with a maximum height of about 0.2 m, reaching the coast of the Kamysh-Burun Bay and further, dissipating through the strait.

Figure 4 shows histograms for the maximum values of wave heights along the western and eastern coasts of the Kerch Strait. The wave heights at latitude 45.3° at the western shore (Fig. 4.1) and 45.2° at the eastern shore (Fig. 4.2) correspond to the maximum fixed rise of the water level at the left and right edges of the bridge, respectively. As follows from the graph, for the left edge this value was 1.5 m, for the right 2 m.

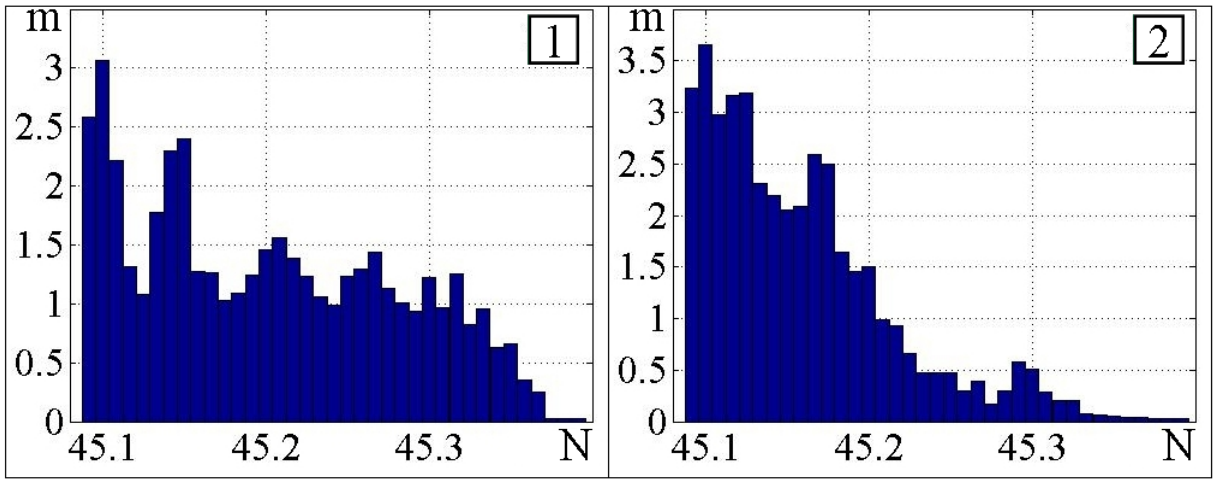

F*ig. 4. Histogram of maximum tsunami heights on a 3-meter isobate for the coast of the Kerch Strait near the Crimean bridge; panel (1): the west coast of the strait; panel (2): east coast of the strait.*

CONCLUSION

The results of the numerical simulation demonstrate that when tsunami waves pass through the Kerch Strait caused by potential strong underwater earthquakes in the Black Sea (with magnitude M ~ 7), the possible wave heights in the Crimean bridge area can be in the 1.5-2 m interval. After 45 min after the start of generation to the eastern supports of the Crimean bridge in the area of the Tuzla spit, a tsunami wave with a relatively small height of the order of 1 m is suitable - the destructive energy of the tsunami was considerably decreased by the Tuzla spit, it is a natural dam. After 1 hour and 45 minutes after the tsunami is generated, a crest of a wave up to a meter high approaches the middle of the bridge, while the left side of the wave front attacks the western part of the bridge that surrounds the Ak-Burun cape. The speed of the water flow in the vicinity of the western bridge supports, circumambulating the cape Ak-Burun, can reach 50 km / h. For the case of the passage of the tsunami along the Strait from Azov to the Black Sea, the maximum wave height in the strait is much smaller, of the order of ~ 0.5 m. It is significant that the wave front, both along the Chushka spit and directly on the bridge, is of flat shape. This leads to a significant loss of energy waves when it attacks the southern coast of the Taman Gulf, so that the wave height in the area of the Crimean bridge is further reduced. In comparison with the case of the passage of the Black Sea tsunami, a wave of elevation from the Sea of Azov attacks the bridge supports across the entire width from the Tuzla spit in the east to the Ak-Burun cape in the west. Thus, the numerical simulation of the generation and propagation of the Black Sea and Azov tsunami caused by potential underwater earthquakes has shown relatively low wave heights in the Crimean bridge area, which is consistent with the few observational data available and the results of other authors.

ACKNOWLEDGEMENTS

This work was supported by the grant of the President of the Russian Federation No. NSh-2685.2018.5.

REFERENCES

1. Grigorash Z.K. A Survey of Remote Mareograms of Some Tsunamis in the Black Sea, Tr. SakhKNII Far-Eastern Branch of the Academy of Sciences of the USSR. - Yu.-Sakhalinsk: SakhKNII, 1972. - Issue. 29. - P. 271-278.
2. Eremeev V.N., Ivanov V.A., Il'in Yu.P. Oceanographic conditions and ecological problems of the Kerch Strait, Marine Ecological Journal. – 2003. V.2, No.5, P.27-40.
3. Shnyukov E.F., Mitin L.I., Tsemko V.P. Accidents in the Black Sea, The publishing company "Manuscript", Kiev, Ukraine. - 1994. - 296 p.
4. Nikonov A.A. Tsunami on the shores of the Black and Azov Seas, Izvestiya RAN: Physics of the Earth. - 1997. - No. 1. - P. 86-96/
5. Pustovitenko B.G., Kulchitsky V.E. Seismicity of the Black Sea Depression, Geophysical Journal. - 1991. - No. 3. - P. 14-19.
6. Solov'eva O.N., Kuzin I.P. Seismicity and tsunami of the north-eastern part of the Black Sea. Oceanology, 2005. - v.45. - №6. - P.826-840.
7. Dotsenko S.F., Ingerov A.V. Numerical analysis of propagation and amplification of tsunami waves of seismic generation in the Azov Sea, Marine Hydrophysical Journal, 2011. - №5. - P. 3-13
8. Dotsenko S.F. The assessment of the level of tsunami hazard of the Black Sea, Bulletin of Moscow University. Series 3. Physics. Astronomy. - 1998. - № 4. - P.19-23.
9. Dotsenko, S.F. Estimates of tsunami wave parameters along the southern coast of the Crimean peninsula, Marine Hydrophysical Journal. 2005. № 3. Pp. 3-10.
10. Polubok T.N. The study of the processes of lithologic-geomorphological changes in the bottom of the Kerch Strait, News of the Odessky state eco-logical university - 2013. - No. 15. - P. 187-196.
11. Wells D.L., Coppersmith K.J. New empirical relationships among magnitude, rupture length, rupture width, rupture area, and surface displacement, Bull. Seism. Soc. Am. 1994. Vol. 84. P. 974-1002.
12. Lobkovsky L.I., Mazova R.Kh., Kolchina E.A. Estimates of the maximum tsunami wave heights for the coast of Sochi under possible strong underwater earthquakes // Doklady of the Academy of Sciences. 2014, 456, No. 5. - P. 604-609.
13. Mazova R.Kh., Tresvyatskaya E.A. Numerical Simulation of Long Water Wave Generation by Dynamic Seismic Source and Their Propagation for Black Sea Basin Russ. J. Earth Sci. V.8, ES6003, doi:10.2205/2006ES000214 http://dx.doi.org /10.2205/ 2006ES000214, (2006)
14. Sielecki A., Wurtele M. The numerical integration of the nonlinear shallow water equations with sloping boundaries, J. Comput. Phys., 6, 219, 1970 doi:10.1016/0021- 9991(70)90022-7.

ISSN 8755-6839

SCIENCE OF **TSUNAMI HAZARDS**

Journal of Tsunami Society International

Volume 37 **Number 4** **2018**

SOURCE PARAMETER ESTIMATES OF THE 4 NOVEMBER 2016 m_b= 4.7 EARTHQUAKE NEAR LAWU MOUNTAIN IN EAST JAVA, INDONESIA

Madlazim[1,2] **and T. Prastowo**[1,2]

[1] Physics Department, Faculty of Mathematics and Natural Sciences, Universitas Negeri Surabaya, Kampus Unesa Ketintang, Surabaya 60231, Indonesia
[2] Center for Earth Science Studies, Faculty of Mathematics and Natural Sciences, Universitas Negeri Surabaya, Kampus Unesa Ketintang, Surabaya 60231, Indonesia
madlazim@unesa.ac.id

ABSTRACT

Due to its geological conditions, Indonesia is home for a series of active volcanoes and fault zones spanning over the Sunda-arc in the country. With respect to possible volcano eruptions, earthquakes, and tsunamis, recent research development has therefore covered areas (previously not classified into areas vulnerable to potential threats)that are possibly suffering from tectonic movement. These include regions in the northern East Java, where Mount Lawu exists. This work aims to estimate source parameters of the 4 November 2016 earthquake with m_b= 4.7 that occurred in the region of interest. The methods were seismic data inversions using full moment tensors implemented in a MTINV software, where waveforms provided by 4 local stations from IA network: PCJI, UGM, SMRI, and KMMI were used. The results show a seismic moment of 5.03 x10^{22} dyne cm, corresponding to a moment magnitude of M_w4.40, variance reduction of 60.8% with a 0.9% ISO component, a 73.8% CLVD component and 25.3%, DC component, and a centroid depth of 33 km. These suggest a complex fault interaction in the source mechanisms with the volcanoes earthquake is found to be complex interaction between fault about mountain Lawu and mountain Lawu.

1. INTRODUCTION

Identification of seismic signals produced by natural earthquakes of either tectonic or volcanic origin is of importance, in particular whenever there is a mountain situated nearby an active fault zone [1]. This problem drew particular attention to the community when an earthquake of $m_b = 4.7$ occurred on Friday, November 4, 2016, at 05:08:12 UTC in a mountain located at Mount Lawu fault zone, stretching across the border of two provinces, the Central and East Java, in Indonesia [2]. As officially reported by The Indonesian Agency for Geophysics, Climatology, and Meteorology (BMKG), such an event was epicentered at 7.60 S and 111.30 E and mostly influenced surrounding cities, including Madiun, Trenggalek, Yogyakarta, Magetan, and Ngawi. Since then, a question of whether the quake is sourced from tectonics- or magma-driven activities has been raised with caution in that the affected regions along the northern part of Java island are not previously considered as regions vulnerable to seismic hazards, as opposed to most areas in the southern Java as part of the more active Sunda-Banda arc [3].

For a better understanding of Earth's crustal deformation processes in areas largely influenced by the Baribis-Mount Lawu thrust system that stretches across the northern Java island, a careful study [4] based on field measurements using Global Positioning System (GPS) has been performed. This study poses a question of whether the thrust system may extend to a more active fault zone in the Flores Sea. With respect to this, there is a need to examine events with relatively small to moderate magnitudes that occur in East Java, where Mount Lawu exists. This examination focuses on the determination of a seismic moment tensor, source parameters and corresponding mechanisms, and a focal centroid depth. Extraction of the source parameters from these earthquakes in the region of interest is of significance as they are too small to be detected by the Global Centroid Moment Tensor (CMT) solutions [5] and hence there have been so far no disseminations on this topic of research with a high local content. Further, the method of moment tensor inversion developed for the case considered in the present study serves as a useful tool for broad analyses of seismograms given by a local network of observatories. However, this method has also been applied to various cases using a regional network of stations [6] with the focus on examining the geological structure and seismicity in Egypt [7], exploring geothermal location in California, US [8], and characterizing nuclear explosions [9].

Within the context of seismic hazard assessment in the northern part of East Java, which includes Surabaya as the second largest city in Indonesia with a population of approximately 3 million people and considering that fault thrust passes through this crowded city and traverses a total distance of 300 km long in East Java, the main purpose of the present work is to estimate source parameters of the 4 November 2016 event with a recorded body wave magnitude of $m_b = 4.7$ that propagated from the source region in the western Mount Lawu zone, East Java. In the process, we also solve focal and

source mechanisms of the event under consideration. In the light of maximizing awareness of the science of disaster and minimizing disaster risks, the results obtained are used as a cornerstone for reassessing the level of seismic hazards in the regions of interest that include Surabaya and its neighboring cities.

2. METHODS

The methodology used in the present work was given in details in [6]. Here, we provide the saline points of the moment tensor inversion method using broadband seismic signals from seismograms filtered by band-pass filter between 45 Hz and 69 Hz, and recorded at an IA network of 4 local stations managed by BMKG, in collaboration with GFZ. The use of seismic waves at low frequencies provides good estimates of earthquake source parameters as these waves are not much influenced by speed and density variations. A full moment tensor is normally decomposed into three components, namely the double-couple (DC), compensated linear vector dipole (CLVD), and volumetric (isotropic-ISO) components. For determination and examination of source parameters of the 4 November 2016 event, we used a MTINV 3.04 software to only apply a full moment tensor composition, instead of a full moment tensor, assuming that there are no other sources, such as explosions in the source region except natural earthquakes of either tectonic or volcanic origin. Keep in mind, the moment tensor inversions in this work were performed with almost a zero component of net volumetric change.

1. Data collection

The broadband seismic data were collected from the 4 local stations used in this study: PCJI, UGM, SMRI, and KMMI. These stations with their geographical positions relative to the source are listed in table 1 below. The data used in this study are available at http://202.90.198.100/webdc3/.

Table 1. Names of stations used in this study with their epicentral distances.

Network code	Seismic station	Latitude	Longitude	Epicentral distance (km)
IA	PCJI	8.19° S	111.18° E	67
IA/GE	UGM	7.91° S	110.52° E	92
IA/GE	SMRI	7.05° S	110.44° E	113
IA	KMMI	7.04° S	113.92° E	295

In accordance with the broadband data recorded, we applied a one dimensional model of velocity to the proposed method. In the model, speed variations of *P*- and *S*-waves with depth D, wave qualities Q_P and Q_S for each wave component, respectively, and the local density ρ_L were provided, as seen in table 2. The wave qualities Q_P and Q_S are dimensionless, showing criteria of how good the model is. As discussed in [10], a threshold value of 500 for the *P*-wave speed distribution over the depth is provided, above which the corresponding *P*-waveforms from seismograms are assumed to be reliable owing to a minimum noise level and for the same reason a threshold value of 250 for the *S*-wave speed distribution is provided, above which the corresponding *S*-waveforms are reliable.

Table 2. Seismic velocity model for use of seismic data inversions.

D (km)	v_P (km/s)	v_S (km/s)	Q_P	Q_S	ρ_L(g/cc)
0.0	4.8	3.1	500	250	2.4
13.0	5.6	3.2	500	250	2.6
45.0	6.1	3.5	500	250	2.8
700	8.0	4.6	1000	500	3.2

2. ***Data analysis***

Analysis of broadband seismogram data was performed by inverting 3 local waveform components obtained from 4 local stations used in this study to extract the source parameters and corresponding source mechanisms of the earthquake examined.Seismic moment tensor describing the earthquake intensity was decomposed into the full moment tensors component only and in turn this simple decomposition of the full moment tensors component into ISO, DC and CLVD components. This argument is supported by practical applications, where source mechanisms reported by almost all seismic surveillances for examining seismicity in particular areas as well as research findings reported in [8, 11] are primarily based on the decomposition of the full moment tensors component into an of ISO, DC and CLVD components.

3. RESULTS AND DISCUSSIONS

We have applied the full moment tensor inversions using broadband seismograms to estimate the source parameters of an earthquake nearby Madiun that occurred on Friday, November 4, 2016. The results of the data inversions are given in the forms of three correlated figures 1, 2, and 3.

Figure 1 describes curve fitting from both observations and simulations with the 3 local component micro-displacements are symbolized as T, R, and Z for tangential, radial, and vertical components, respectively. In all stations, black-colored curves show waveforms obtained from field observations whereas red-colored ones are for synthetic waveforms. The results of the moment tensor inversions for all the broadband seismograms recorded by 4 local stations can be seen on the top right of figure 1, where all numerical values characterizing the event, such as geographical locations in longitude and latitude degrees, a centroid depth in km, nodal planes (NP1 and NP2), a seismic moment (M_o), and all 6 components of the momen tensors(M_{xx}, M_{xy}, M_{xz}, M_{yy}, M_{yz}, M_{zz}) with the other 3 components are given in a set of paired tensors $M_{yx} = -M_{xy}$, $M_{zx} = -M_{xz}$, and $M_{zy} = -M_{yz}$ as they are symmetric tensors.

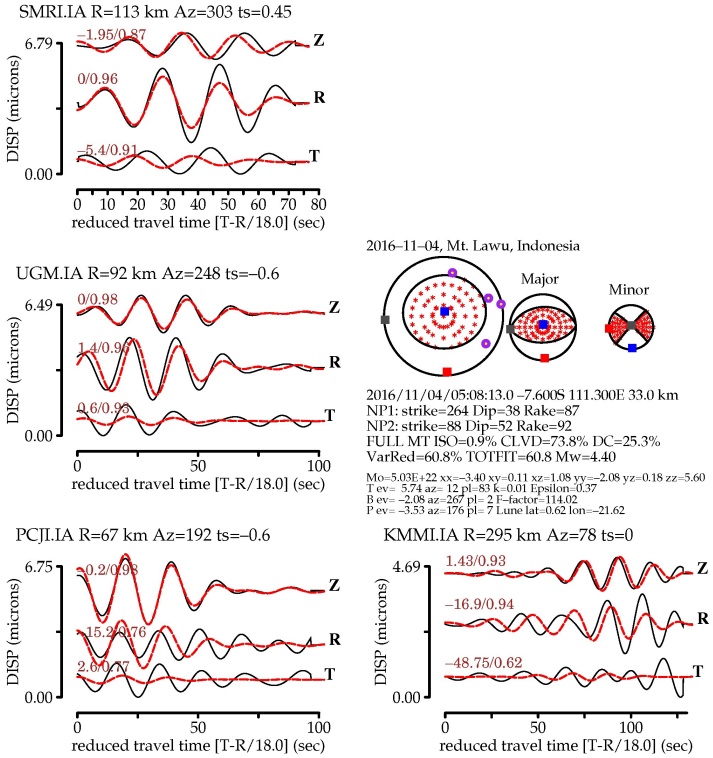

Figure 1. *Broadband seismogram data with all the 3 local Z, R, and T waveform components from the 4 November 2016 event, showing curve fittings of observed and simulated waveforms obtained from the 4 local stations (PCJI, UGM, SMRI, KMMI) used in the present study, where black colors represent the observed waveforms and red colors represent the simulated waveforms. On the top right are the results of the moment tensor inversions for the full moment tensors component decomposition, where all computed values corresponding to the seismic source parameters are provided, including the source mechanisms and focal centroid depth. Numerical values above 3 waveform components recorded at each station denote epicentral distance R from the source, azimuthal location Az, and times ts at which the seismic inversion started to run.*

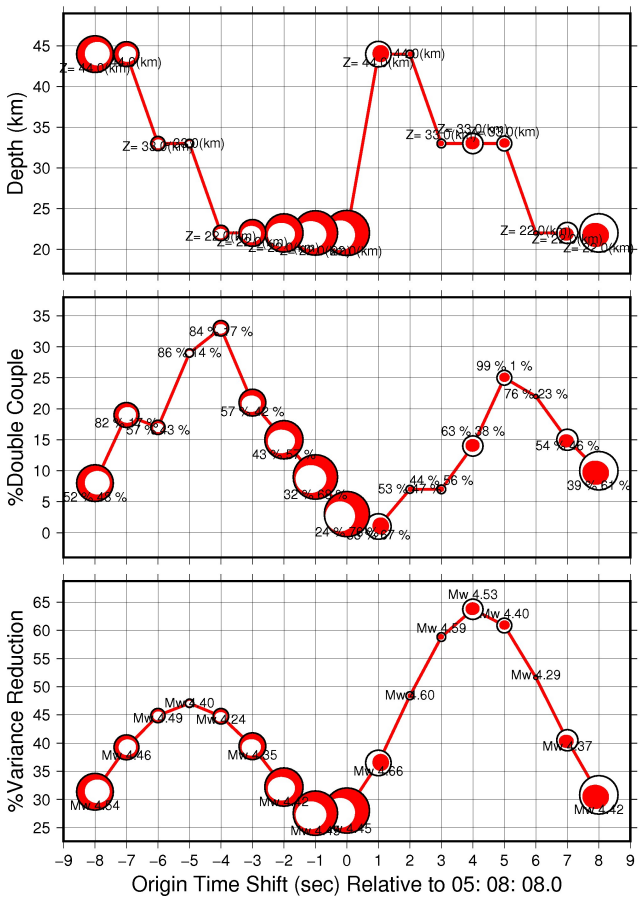

Figure 2. *Visual graphics, showing cross-correlation of variance reduction, full moment tensors component, and centroid depth with respect to time taken for the moment tensor inversions. The variance reduction is at its peak of 60.8% corresponding to a seismic moment of M_w 4.40 (bottom panel), which correlates to a 25.3% DC component (middle panel) and a 33 km centroid depth (top panel). This cross-correlation shows that the 4 November 2016 earthquake in the Mount Lawu fault zone is a seismic event caused by a complex interaction of both tectonic and volcanic forces, with the vertical CLVD component (73.8%) being the leading process in the source mechanisms.*

From statistical analysis of the data fitting, the moment tensor inversions yield variance reduction of 60.8% that corresponds to a seismic moment magnitude of M_w 4.40, a 0.9% an ISO, 25.3% DC component and a 73.8% vertically oriented CLVD component, and a focal centroid depth of 33 km. The almost zero ISO component for a relatively shallow source in the present case is consistent with previous finding [11], where the isotropic component was reported as independently unresolved from the CLVD component for major deep earthquakes. These calculations demonstrate the relative

importance of the presence of volcanic over pressure with almost no volumetric component observed in the source mechanisms, similar to the one discussed in [12] for the unusual 1996 Bardarbunga event that occurred in Iceland. These findings reflect unresolved, complicated processes in nature as claimed by previous work, see for example, [2, 4, 6].

The possible source for the 4 November 2016 earthquake seems to have dual mechanisms due to the complex interactions of the fault thrust and volcanic depression system, where the volcanic depression plays a greater role in regard to the larger CLVD component in percentage (73.8%), relative to the DC component (25.3%). This is consistent with the results of both primitive [3] and modern work [2, 4], claiming that areas of convergence based on geological and volcanic arc history are found along the fault lines across the border of Central and East Java. As conclusively noted by [2] based on the stratigraphic records of a volcanic eruption, Java is thus fundamentally a volcanic island with its recorded long history of arc volcanism.

Plotted in figure 2, visual graphics as a result of the seismic moment tensor inversions. The plots show cross-correlation of statistical variance reduction (in percent), an ISO, DC, CLVD component (in percent), and a centroid depth (in km). The 4 November 2016 event fits with a peak of variance reduction at 60.8%, corresponding to a seismic moment magnitude of M_w 4.40, accompanied by many earthquakes with portions of ISO, DC) and CLVD components are somewhat in balance where the NDC component is dominated by the vertical CLVD. As with natural earthquakes having almost a zero volumetric (ISO) component, the source mechanism is commonly modeled using a combined (DC + CLVD) source mechanism, as also discussed in [8, 11]. This combination, as in most cases, places the DC component in a major role but in a particular example, such as the 1996 Bardarbunga earthquake [12], the volumetric (ISO) component was insignificant, making the CLVD component to be the dominant part and hence a less role in the DC component. These, together with the results of both moment tensor inversions (figure 1) and cross-correlation (figure 2), yield the same centroid depth of 30 km, suggesting an uplift magma-driven motion of fluid flow under the influence of high pressure inside a mountain chamber [6], as oppose to the processes characterizing underground explosions with domination of the apparent isotropic component [9].

In summary, we have utilized the broadband seismogram data from the 4 local seismic stations (within the IA network) surrounding the epicenter of the 4 November 2016 event of m_b = 4.7 that occurred in the potential active Mount Lawu fault zone in East Java. The moment tensor inversions applied to the broadband data result in a vertically oriented CLVD component as a relatively dominant feature in the source mechanisms with almost no isotropic component (figure 3). This suggests that depression inside Mount Lawu mountain is a leading uplift force although it is not yet clear why there exists somewhat a dynamic balance between the DC (25.3%) and CLVD components (73.8%). However, the moment tensor inversions give better resolution in determining a focal centroid depth

for the source than other methods of depth estimation, particularly when dealing with potential an complex interaction a mountain situated nearby an active mountain Lawu as is the case in the present work.

In addition, determination of earthquake source parameters using the moment tensor inversion method is of importance as the method is likely to be able to reveal the dominant factor of the source. It follows that using this method accurate identification of seismic source characteristics whether it is of tectonic or volcanic origin, or due to underground explosions or surface landslides is relatively easy to handle [5, 7]. As pointed out by [1], the identified source parameters and focal mechanisms can also be used to determine whether the earthquake is classified intraplate (when the centroid location is at or nearby the source region) or extrapolate (when the centroid is located at relatively far from the source).

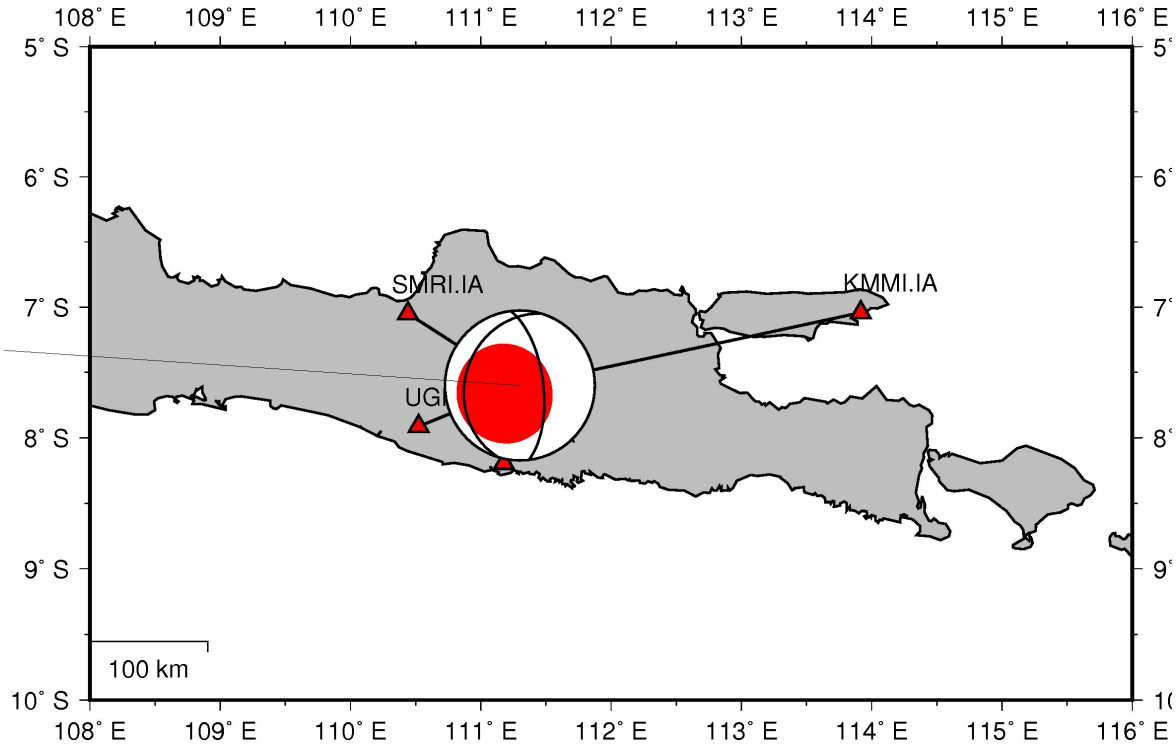

Figure 3. A simple map, showing type of source mechanisms for the 4 November 2016 earthquake (given in the form of a beach-ball slightly dominated by vertical CLVD component, relative to the DC component) with all of the 4 local seismic stations (PCJI station is unseen due to an excessive size of the beach-ball) used in the present study. The focal mechanism is vertical-P of CLVD. The vertical-P focal mechanisms indicate that the earthquakes are associated with a documented episode of volcanic unrest at a nearby volcano [13], where unrest is not soon followed by an eruption [14].

4. CONCLUSIONS

We have performed the full moment tensor inversions for the 4 November 2016 earthquake of m_b = 4.7 that occurred about mountain Lawu zone, East Java, Indonesia. This event raises a crucial question whether such an event was mainly triggered by seismo-tectonic forces or induced by magma-driven activities. Using the data from broadband waveforms recorded at local stations within an IA network, the method of the moment tensor inversions reveals surprising results, providing a new insight into the source and focal mechanisms of the quake under consideration. The results indicate the dominance of the ISO component (0.9%), compensated linear vector dipole (CLVD) component (73.8%) relative to the double-couple (DC) component (25.3%), suggesting no net volumetric-isotropic (ISO) component, which is a puzzling result from a volcanic point of view [12]. Together with a measured seismic moment of 5.03 x10^{22} dyne cm corresponding to M_w 4.40 (an intermediate earthquake in size) and a relatively shallow, centroid depth of 33 km, we conclude from the relative dominance of the CLVD component over DC component that the 4 November 2016 event is not merely related to the active mountain Lawu zone. Instead, the event is primarily driven by complex internal interactions between active faults and volcanic systems of depression, normally characterizing intraplate earthquakes nearby the mountain Lawu zone.

However, the main finding in the current study raises a possibility for crustal deformation to occur in the eastern Sunda-Banda arc owing to earthquakes (with and with no tsunamis generated) in areas in the northern Central and East Java, previously not considered as regions vulnerable to either tectonic or volcanic earthquakes. As suggested by [4], potential active crustal structures beneath the island of Java and hence the presence of active fault zones particularly in the northern part of Java may induce several devastating ruptures in the past times. Thus, much concern with care about the importance of considering crustal deformation and fault activity in East Java, as a region of interest, is necessary for minimizing disaster risks, highlighting the need for reconsidering the level of seismic hazards as part of future seismic analysis and assessment in the surrounding regions.

ACKNOWLEDGMENTS

The authors would sincerely like to thank The Indonesian Agency for Geophysics, Climatology, and Meteorology (BMKG) for its supports in the form of seismograms available from IA network for use in this work and also thank Dr. Ichinose for permitting us to use an MTINV 3.04 software for seismic data inversions.

REFERENCES

[1] Kasmolan M, Santosa B J, Lees J M and Utama W 2010 Earthquake source parameters at the Sumatran fault zone: identification of the activated fault plane. Cent. Eur. J. Geosci. 2(4) 455-74

[2] Smyth H R, Hall R and Nichols G J 2008 Cenozoic volcanic arc history of East Java, Indonesia: the stratigraphic record of eruptions on an active continental margin *Geol. Soc. Am.* **436** 199-222

[3] Van Bemmelen R W 1949 *The Geology of Indonesia* vol 1A (The Hague: Government Printing Office) 732 p

[4] Koulali A, McClusky S, Susilo S, Leonard Y, Cummins P, Tregoning P, Meilano I, Efendi J and Wijanarto A B 2016 The kinematics of crustal deformation in Java from GPS observations: implications for fault slip partitioning *EarthPlanet. Sci. Lett.* **458** 69-79

[5] Mohamed G-E A and Omar K 2014 Source parameters and moment tensor of the ML 4.6 earthquake of November 19, 2011, southwest Sharm El-Sheikh, Egypt *J.Astron. Geophys.* **3** 27-36

[6] Ichinose G A, Anderson J G, Smith K D and Zeng Y 2003 Source parameters of eastern California and western Nevada earthquakes from regional moment tensor inversion *Bull.Seismol. Soc. Am.* **93**(1) 61-84

[7] Abdelazim M, Samir A, El-Nader I A, Badawy A and Hussein H 2016 Seismicity and focal mechanisms of earthquakes in Egypt from 2004 to 2011 *J. Astron. Geophys.* **5** 393-42

[8] Boyd O S, Dreger D S, Lai V H, and Gritto R 2015 A systematic analysis of seismic moment tensor at the geyser geothermal field, California *Bull. Seismol. Soc. Am.* **105(5)** 2969-86

[9] Chiang A, Dreger D S, Ford S R, Walter W R 2014 Source characterization of underground explosions from combined regional moment tensor and first-motion analysis. *Bull.Seismol. Soc. Am.* **104**(4) 1587-600

[10] Minson S E, Dreger D S, Bürgmann R, Kanamori H and Larson K M 2007 Seismically and geodetically determined nondouble-couple source mechanisms from the 2000 Miyakejima volcanic earthquake swarm *J. Geophys. Res.* **112** B10308 doi: 10.1029/2006JB004847

[11] Kawakatsu H 1996 Observability of the isotropic component of a moment tensor. *Geophys. J. Int.* **126**525-44

[12] Tkalcić H, Dreger D S, Foulger G R and Julian B R 2009 The puzzle of the 1996 Bárdarbunga, Iceland, earthquake: no volumetric component in the source mechanism *Bull. Seismol. Soc. Am.***99**(5) 3077-85

[13] Ashley Shuler, Meredith Nettles, and Göran Ekström 2013. Global observation of vertical-CLVD earthquakes at active volcanoes. JOURNAL OF GEOPHYSICAL RESEARCH: SOLID EARTH, VOL. 118, 138–164, doi:10.1029/2012JB009721.

[14] Moran, S. C., C. Newhall, and D. C. Roman (2011), Failed magmatic eruptions: Late-stage cessation of magma ascent, Bull. Volcanol., 73, 115–122, doi:10.1007/s00445-010-0444-x.

ISSN 8755-6839

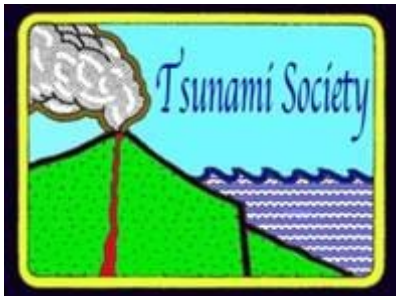

SCIENCE OF TSUNAMI HAZARDS

Journal of Tsunami Society International

Volume 37 **Number 4** **2018**